European Journal of Medicinal Chemistry 265 (2024) 116114

Contents lists available at ScienceDirect

European Journal of Medicinal Chemistry

journal homepage: www.elsevier.com/locate/ejmech

Research paper

An ^{19}F NMR fragment-based approach for the discovery and development of BRCA2-RAD51 inhibitors to pursuit synthetic lethality in combination with PARP inhibition in pancreatic cancer

Samuel H. Myers [a,1], Laura Poppi [b,1], Francesco Rinaldi [a,b,1], Marina Veronesi [c,d], Andrea Ciamarone [a], Viola Previtali [a], Greta Bagnolini [b], Fabrizio Schipani [a], Jose Antonio Ortega Martínez [a], Stefania Girotto [a,c], Giuseppina Di Stefano [e], Fulvia Farabegoli [b], Naomi Walsh [f], Francesca De Franco [g], Marinella Roberti [b,*], Andrea Cavalli [a,h,**]

[a] Computational and Chemical Biology, Istituto Italiano di Tecnologia, 16163, Genoa, Italy
[b] Department of Pharmacy and Biotechnology, University of Bologna, 40126, Bologna, Italy
[c] Structural Biophysics Facility, Istituto Italiano di Tecnologia, 16163, Genoa, Italy
[d] D3 PharmaChemistry, Istituto Italiano di Tecnologia, 16163, Genoa, Italy
[e] Department of Surgical and Medical Sciences, University of Bologna, 40126, Bologna, Italy
[f] School of Biotechnology, Dublin City University, D09 NR58, Dublin, Ireland
[g] TES Pharma S.r.l., I-06073, Corciano, Perugia, Italy
[h] Swiss Federal Institute of Technology Lausanne (EPFL), Switzerland

ARTICLE INFO

Keywords:
Synthetic lethality
BRCA2-RAD51
PARP inhibition
NMR fragment-based screening
Pancreatic cancer

ABSTRACT

The BRCA2-RAD51 interaction remains an intriguing target for cancer drug discovery due to its vital role in DNA damage repair mechanisms, which cancer cells become particularly reliant on. Moreover, RAD51 has many synthetically lethal partners, including PARP1-2, which can be exploited to induce synthetic lethality in cancer. In this study, we established a ^{19}F-NMR-fragment based approach to identify RAD51 binders, leading to two initial hits. A subsequent SAR program identified **46** as a low micromolar inhibitor of the BRCA2-RAD51 interaction. **46** was tested in different pancreatic cancer cell lines, to evaluate its ability to inhibit the homologous recombination DNA repair pathway, mediated by BRCA2-RAD51 and trigger synthetic lethality in combination with the PARP inhibitor talazoparib, through the induction of apoptosis. Moreover, we further analyzed the **46**/talazoparib combination in 3D pancreatic cancer models. Overall, **46** showed its potential as a tool to evaluate the RAD51/PARP1-2 synthetic lethality mechanism, along with providing a prospect for further inhibitors development.

1. Introduction

DNA damage repair is a vital process in the continued lifecycle of the cell. Depending on the type of damage, the DNA damage response (DDR) network orchestrates the activation of multiple repair pathways to ensure that these errors are not passed down upon cell division. Cancer genomic instability often causes defects in the DDR machinery [1]. In turn, the resulting genetic abnormalities can make cancer cells particularly dependent on specific DDR mechanisms [2]. This presents an opportunity for selective anticancer treatments [3]. Targeting DDR pathways offers the opportunity to leverage synthetic lethality (SL), as part of the toolbox of precision medicine, to develop anticancer therapies. Two genes are synthetically lethal if the perturbation of either of them is viable, while the simultaneous impairment of both genes results in cell death [4]. If a synthetically lethal gene pair is essential for cancer cells survival, inhibiting both of these genes or their products would selectively kill cancer cells [5]. The best example of SL in the clinic is the administration of PARP inhibitors (PARPi) in BRCA1/2-defective

* Corresponding author.
** Corresponding author. Computational and Chemical Biology, Istituto Italiano di Tecnologia, 16163 Genoa, Italy
E-mail address: marinella.roberti@unibo.it (M. Roberti).
[1] Authors equally contributed to this work.

https://doi.org/10.1016/j.ejmech.2023.116114
Received 27 October 2023; Received in revised form 29 December 2023; Accepted 30 December 2023
Available online 31 December 2023

tumors. So far, six PARPi, olaparib, rucaparib, niraparib, fuzuloparib, pamiparib, and talazoparib (TLZ), have received regulatory approval across several tumor types, including ovarian [6], breast [7], pancreatic [8], and prostate cancers [9]. However, despite their revolutionary breakthrough, PARPi are still restricted to the minority of oncology patients who present with BRCA1/2 mutations.

A major role of BRCA2 is the recruitment of RAD51, an evolutionally conserved recombinase that acts as a key player in the repair of double-strand breaks (DSBs) through homologous recombination (HR). RAD51 is positively upregulated in several tumor types, and its high expression is widely associated with resistance to traditional chemotherapies and radiotherapies that rely on DNA damaging agents [10,11]. This contributes to make RAD51 an attractive target for anticancer therapeutics.

Over the last years, our group has pursued the development of small molecule inhibitors of the BRCA2-RAD51 interaction to induce SL in combination with PARPi [4,12,13]. Leveraging *in silico* methods, in particular virtual screening (VS) corroborated by molecular docking studies, we have performed structure-based design and developed different a series of BRCA2-RAD51 inhibitors, including 1,2,4-triazoles [13] and dihydropyrazolines [4]. To do this, we have used the available PDB structure of the RAD51-BRC4 complex (PDB entry: 1N0W) [14], where BRC4 refers to the BRCA2 amino acid sequence with the highest affinity for RAD51. Interestingly, Scott et al. [15] has recently combined fragment-screening and structure-based fragment approach to develop a promising hit compound, CAM833, able to mimic the FXXA domain of BRC4 and strongly impair the BRCA2-RAD51 interaction [15]. Going beyond computational-assisted methods, our group probed the applicability of RAD51 in protein-templated dynamic combinatorial chemistry (ptDCC) to attempt the identification of novel RAD51 ligands [16]. Overall, BRCA2-RAD51 interaction has been studied in a variety of medicinal chemistry approaches. Ligand Based Nuclear Magnetic Resonance (NMR) has been successfully exploited for the hit identification in Fragment-Based Drug Discovery (FBDD) [17–19]. Advantages of FBDD include a more intensive exploration of chemical space, the use of high-throughput screenings and the collection of insights towards protein-ligand molecular behavior [20]. A similar approach has already been successfully pursued to identify fragments able to disrupt the BRC4-RAD51 interaction exploiting a chimeric RadA-RAD51 construct [21] Nevertheless, to the best of our knowledge no NMR fragment-based screening on the full-length wild type form of human RAD51 (RAD51 WT) has been performed, so far. Therefore, we decided to exploit RAD51 WT and carry out a ^{19}F NMR fragment-based screening [22,23] aimed at identifying novel hits able to disrupt the RAD51-BRC4 interaction, to be eventually developed into a lead compound. Upon the identification of two hit compounds, SAR studies generated two distinct series, deriving from different chemotypes. Among the synthesized compounds, **46** possessed the most appealing biological profile, inhibiting BRCA2-RAD51 in biophysical/biochemical assays and synergizing with the PARPi TLZ in both 2D and 3D models of pancreatic cancer.

2. Results and discussion

2.1. Hit identification via ^{19}F T_2 filtered NMR fragment-based screenings

The ^{19}F T_2 filter NMR is a robust and sensitive method to perform fragment-based screening campaigns, enabling the identification of even very weak inhibitors [16–18,24,25]. As interest has grown in the technique, specific ^{19}F labeled fragments libraries, such as the Local Fluorine-Environment (LEF) library [19], have been developed. Taking advantage of our in-house fluorinated fragment library, built following the LEF approach, we performed a NMR fragment-based screening on RAD51 WT, which shows an intrinsic tendency to form self-assembled oligomeric structures, necessary for its physiological function [26]. Given the dynamic oligomeric arrangement of RAD51 WT, we initially evaluated protein stability and aggregation testing a mixture of 20-fluorinated fragments in the absence and presence of RAD51 WT at t_0 and after 48 h (t_1) by ^{19}F T_2 filter NMR experiments (Fig. S1). In these experiments, the binding of a compound to a protein induces a line broadening of its signal coupled with a consequent decrease in its intensity. Diffuse binding effects, observed when testing a mixture of compounds, suggest that the protein is unstable and tend to aggregate. In the preliminary experiments performed on RAD51 WT, only one of the 20 ^{19}F fragment signals was affected by protein addition suggesting that one fragment was bound to RAD51 WT. Nevertheless, for the other 19 fragments no diffused, non-specific bindings were observed. The NMR signals of all fragments were stable in time for at least 48 h after protein addition. These preliminary ^{19}F NMR experiments performed on 20 fragments enabled us to identify one RAD51 WT binder and assess that the protein is stable under the experimental tested conditions. Having confirmed the suitability of RAD51 WT for the screening, 200 fluorinated fragments were later screened for binding in mixtures of 20–25 compounds each in the absence or presence of RAD51 WT by ^{19}F T_2 filter NMR experiments. Ten hits were identified, which were further confirmed in single binding experiments performed in the presence of a non-binder fragment **1** selected from the initial screening, as a negative control. Subsequently, ^{19}F NMR T_2 competition experiments [22] in the presence of BRC4 peptide were performed on these ten compounds in order to gauge their ability to disrupt the RAD51-BRC4 interaction (Fig. 1). Interestingly, only three (**2**, **3**, **4**) of the identified ten fragments were displaced by BRC4 as highlighted by the significant sharpening of their ^{19}F NMR signals after peptide addition to the RAD51-compounds complex (Fig. 1). As expected, no variation in the ^{19}F signal of the negative control **1** is observed either in the presence of protein or protein and peptide.

Compound **4** was not further studied due to its small size and non-drug like properties, while **2** and **3** were considered more suitable for further optimization. **2** and **3** were then further tested for their ability to disrupt the RAD51-BRC4 interaction using a competitive biochemical ELISA assay previously reported by Rajendra and colleagues [27]. This assay confirmed that compound **3** can bind RAD51 WT and efficiently displace BRC4 in low micromolar range (Table 1). Conversely, the ELISA assay did not detect any displacement effect for **2**. Our working hypothesis is that compounds disrupting RAD51-BRCA2 should affect HR repair. For this reason, we used a commercially available assay to evaluate the ability of **2** and **3** to inhibit HR in pancreatic ductal adenocarcinoma (PDAC) BxPC-3 cells (HR Quick Assay, HR-QA) (Experimental Section 4.4.4), as reported in our previous studies [4, 13]. For fragment **2** we could measure HR at different concentrations (Fig. S2) and calculate an IC_{50} value, while for fragment **3** we could only observe a 40 % HR inhibition at doses ranging from 30 to 600 μM (Table 1).

All together these data suggested **3** was a good starting point for the further SAR development. Unfortunately, the difficulties in achieving a high-resolution 3D structure of RAD51 in complex with its inhibitors did not allow to have the compounds binding poses in the protein structure, thus hampering a structure-based development of the identified hits. Indeed, we were not able to obtain protein crystals of the fully human monomeric form of RAD51 most likely due to its flexible N-terminal domain [28]. Moreover, as reported in the literature, attempts to increase the humanization of chimeric RadA-RAD51 constructs reduced the chances to obtain protein crystals, suggesting that even the crystallization of the isolated RAD51 C-terminal domain is rather challenging [29]. Nevertheless, in light of the promising in vitro and in cell data obtained, we decided to start an explorative medicinal chemistry campaign to investigate the effects of substituents at positions 3, 5, and 7 of fragment **3** (Fig. 2).

2.2. Chemical exploration of fragment 3

Fragment **3** was functionalized around its 1,2,3-triazole-fused pyrimidine scaffold, by modifying three different regions, the phenyl ring (R^1), the trifluoromethyl group (R^2) and the hydroxyl group (R^3)

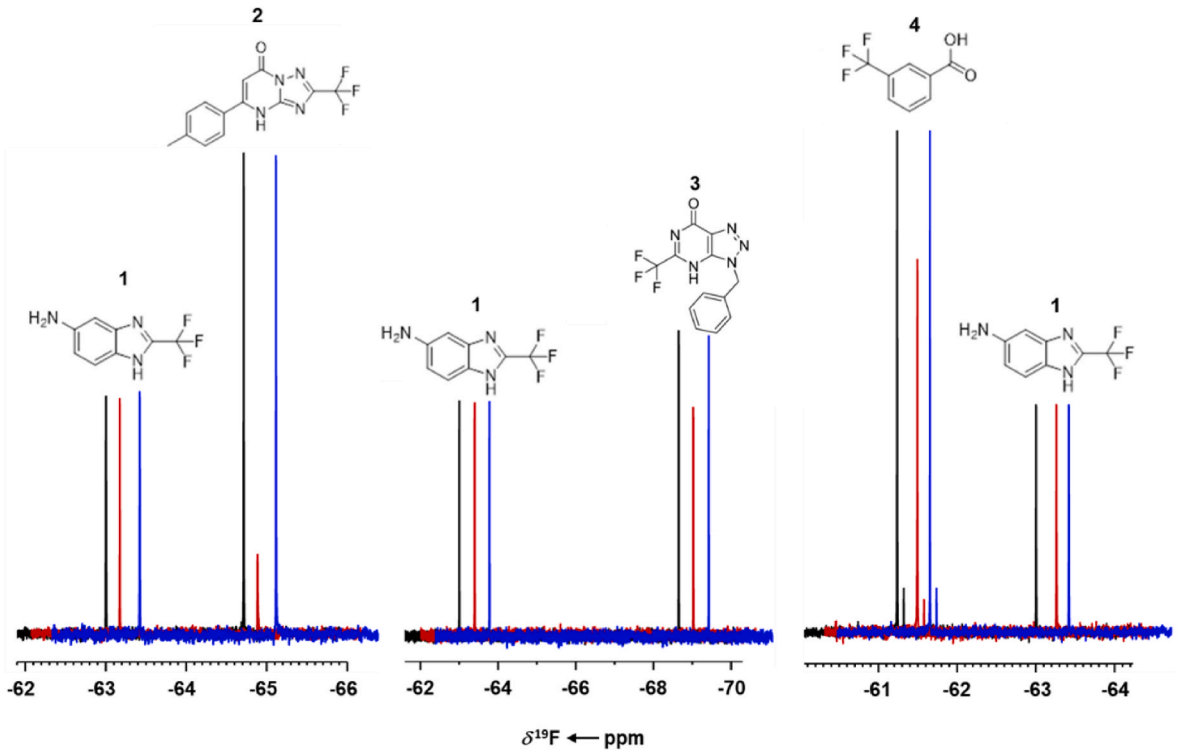

Fig. 1. ^{19}F T_2 filter NMR competition experiments of compounds **2** (left), **3** (middle) and **4** (right) in the absence (black) and in presence of 1 μM RAD51 WT (red), or 1 μM RAD51 WT + 20 μM BRC4 (blue). The signals of compounds **2** and **3** and **4** strongly decreased in the presence of RAD51 WT due to the line broadening of their ^{19}F NMR signals induced by the binding events. The sharpening of compounds **2**, **3** and **4** ^{19}F signals, observed upon addition of BRC4, are due to their displacement from RAD51 WT induced by peptide binding to the protein. **1** is a negative control identified by the initial screening.

Table 1
In vitro evaluation of **3** and **2**.

Fragment	NMR	ELISA [a] (EC_{50} μM)	ELISA [a] (E_{max} %)	%HR inhibition [b]
2	Binder	NA [c]	NA [c]	IC_{50} 369 μM
3	Binder	4	75	40 % at 30 μM

[a] Competitive ELISA assay using biotinylated BRC4 peptide to disrupt the RAD51-BRC4 interaction was performed according to the modified method described by Rajendra et al. [27]; CAM833, a known RAD51-BRCA2 disruptor developed by Scott et al. [15], was used as internal reference compound. E_{max}% refers to the percentage of the maximum activity at 100 μM of the tested compound and compared to the maximum activity of CAM833 at the same concentration.

[b] HR was evaluated by real-time PCR (procedure described in the Experimental Section).

[c] NA = not active.

respectively (Fig. 2). In particular, the phenyl ring (R^1) was para- (**5**–**6**) and ortho-substituted (**7**) or replaced with a cyclohexyl (**8**) and a benzyl moiety (**9**). Then, the CF_3 (R^2) group was replaced with linear and cyclic alkyl groups (**10**–**13**), eventually containing heteroatoms (**14**–**15**), or with unsubstituted (**16**) and para-substituted phenyl ring (**17**–**20**). This was meant to evaluate eventual hydrophobic bonds and the size of the binding pocket. Lastly, the hydroxyl group (R^3) was replaced by an amino group (**20**), small amines (**21**–**22**) and a methoxy group to probe its function as H-bond donor/acceptor. All the synthetic routes are described in Supplementary (Scheme S1–S3). According to the ELISA assay, none of the new derivatives showed an improved profile compared to the parent compound **3**, in terms of EC_{50} and E_{max}. We observed a loss of affinity for RAD51 up to 10-fold for many derivatives, highlighting the detrimental effect caused by those modifications (Table S1). We could argue that all the three explored groups are involved in the interaction with RAD51 and cannot be replaced. However, the fragment was not versatile enough to consider further modifications. For this reason, we attempted a scaffold-hop approach by changing the [1,2,3]triazolo[4,5-*d*]-pyrimidin with a pyrazole[3,4-*d*] pyrimidin (**24**) and a purine core (**25**). The synthetic routes are reported in SI (Scheme S4–S5). Again, the new derivatives showed a dramatic decrease in activity, confirming the importance of the [1,2,3]triazolo [4,5-*d*]-pyrimidin motif.

Considering these results, we decided to reconsider fragment **2,** for further development. Indeed, although **2** was not selected due to its lack of activity in ELISA (Table 1), it was the best performing hit in the ^{19}F NMR experiments (Fig. 1) and was able to inhibit HR in BxPC-3 cells (Table 1). Consequently, we began chemical exploration around fragment **2**.

2.3. Optimization of fragment 2: chemistry and SAR studies

Fragment **2** was further developed in an analogous manner to **3**, by pursuing an exploratory SAR campaign driven by ELISA (EC_{50}, E_{max}) and solubility as preliminary screens (Table 2). Moreover, depending on those results, the new derivatives were tested for HR inhibition (Table 3). The assay was firstly performed at 350 μM as it was close to the IC_{50} of **2** (Table 1). Derivatives showing HR inhibition greater than that shown by **2** were also tested at 20 μM, as this is comparable to our best BRCA2-RAD51 inhibitor, ARN24089, referred to as 35d in previous work (HR inhibition 54 %, 20 μM) [4]. Initial SAR focused around modifying the phenyl ring in addition to introducing other moieties at the R^2 position. The chemical feasibility of this series in general was low and was particularly poor with a CF_3 group at the R^1 position. Thus, reactions with the substituted triazole **26a** and ethyl benzoyl acetates only provided access to the original fragment **2**. Changing the CF_3 group to a methyl (**26b**) allowed for a marginal increase in reactivity, which allowed access to **27**–**31** (Scheme 1).

This first series was then tested in ELISA (Table 2), and three compounds (**28**, **29** and **31**) exhibited activity, with **29** showing a marked

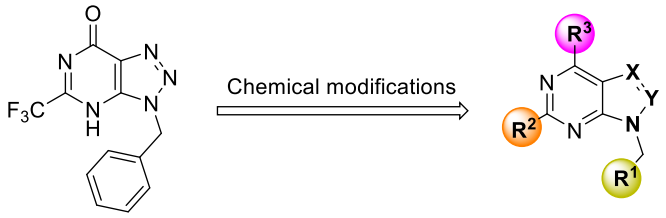

3 5 - 25

3: X = N, Y = N, R^1 = C_6H_5, R^2 = CF_3, R^3 = OH
5: X = N, Y = N, R^1 = 4-Cl-C_6H_4, R^2 = CF_3, R^3 = OH
6: X = N, Y = N, R^1 = 4-Br-C_6H_4, R^2 = CF_3, R^3 = OH
7: X = N, Y = N, R^1 = 3-OCH_3-C_6H_4, R^2 = CF_3, R^3 = OH
8: X = N, Y = N, R^1 = C_6H_{11}, R^2 = CF_3, R^3 = OH
9: X = N, Y = N, R^1 = CH_2-C_6H_5, R^2 = CF_3, R^3 = OH
10: X = N, Y = N, R^1 = C_6H_5, R^2 = $C(CH_3)_3$, R^3 = OH
11: X = N, Y = N, R^1 = C_6H_5, R^2 = CH_3, R^3 = OH
12: X = N, Y = N, R^1 = C_6H_5, R^2 = CH_2CH_3, R^3 = OH
13: X = N, Y = N, R^1 = C_6H_5, R^2 = 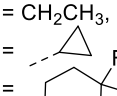 , R^3 = OH
14: X = N, Y = N, R^1 = C_6H_5, R^2 = 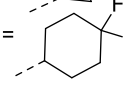 , R^3 = OH
15: X = N, Y = N, R^1 = C_6H_5, R^2 = 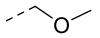 , R^3 = OH
16: X = N, Y = N, R^1 = C_6H_5, R^2 = C_6H_5, R^3 = OH
17: X = N, Y = N, R^1 = C_6H_5, R^2 = 4-Cl-C_6H_4, R^3 = OH
18: X = N, Y = N, R^1 = C_6H_5, R^2 = 4-Br-C_6H_4, R^3 = OH
19: X = N, Y = N, R^1 = C_6H_5, R^2 = 3-OCH_3-C_6H_4, R^3 = OH
20: X = N, Y = N, R^1 = C_6H_5, R^2 = CF_3, R^3 = NH_2
21: X = N, Y = N, R^1 = C_6H_5, R^2 = CF_3, R^3 = $NHCH_3$
22: X = N, Y = N, R^1 = C_6H_5, R^2 = CF_3, R^3 = $NHC(CH_3)_3$
23: X = N, Y = N, R^1 = C_6H_5, R^2 = CF_3, R^3 = OCH_3
24: X = C, Y = N, R^1 = C_6H_5, R^2 = CF_3, R^3 = OH
25: X = N, Y = C, R^1 = C_6H_5, R^2 = CF_3, R^3 = OH

Fig. 2. Chemical exploration of **3** in position R^1, R^2 and R^3 and scaffold-hop.

increase in EC_{50} (10.8 ± 1.3 μM), however these hits were thought to be unreliable as the E_{max} were below an acceptable value of 70 %, when compared to the internal reference compound **CAM833**. In addition, **29** and **31** were tested for their activity against HR inhibition. However, neither compound showed an improvement over **2** (Table 3).

Due to the difficulty in accessing these molecules, and to reduce the number of nitrogen's present in the structure, a scaffold hop was proposed. Two potential scaffolds were considered, pyrazolo[1,5-*a*]pyrimidines and imidazo[1,2-*a*]pyrimidines, however the imidazo[1,2-*a*]pyrimidines derivatives proved inaccessible.

Initially two pyrazolo[1,5-*a*]pyrimidines derivatives of **2** and **27** were prepared by reaction of the pyrazoles **32a** and **32b** in a similar manner to the initial series to yield **33** and **34** (Scheme 2). Immediate improvements were seen in terms of the synthesis with increased yields. Furthermore, these two compounds demonstrated a marked increase in ELISA activity and importantly E_{max} (**33** EC_{50} = 55.5 ± 4.5 μM, E_{max} = 91 % and **34** EC_{50} = 127 μM, E_{max} = 80 %), however a drop in solubility compared to their triazolopyrimidine analogues was notable (Table 2). This emboldened us to continue with this scaffold and begin exploratory SAR around these pyrazolo[1,5-*a*]pyrimidines, attempting to improve ELISA scores while keeping solubility at an acceptable level.

Initial modifications occurred at the C5 position (R^1), utilizing a series of commercially available aminopyrazoles (**32c-h**) with in total seven compounds being prepared (**35–41**) (Scheme 2).

As can be seen in Table 2 larger moieties such as the bulkier aliphatic groups in **38**−**40,** or the bulky thiazole group in **41** were not tolerated due to a large decrease in solubility. Overall, small aliphatic groups seemed to be the most tolerated with CF_3, proton, and ethyl groups showing similar performance in terms of ELISA (Table 2). Compounds **33–37** were progressed to the HR assay, and while **34** and **35** suffered from solubility issues, the other three compounds showed an increase in HR inhibition in respect to **2** at 350 μM concentration (Table 3). When progressed into the 20 μM concentration however, all compounds were inactive aside from **36** which showed minimal activity (Table 3).

In order to investigate the possibility of substituting at the N4 (R^3) position (Scheme 3), alkylations were performed on **33** with alkyl iodides and potassium carbonate in acetone. These were achieved in good yields with alkylation at the pyrimidine nitrogen confirmed by NMR; however, substitution at this position meant that the tautomerism that exists usually on the pyrazolo[1,5-*a*]pyrimidine scaffold was disrupted, this caused a drop in solubility and activity in the ELISA assay, resulting in only methyl (**42**) and ethyl (**43**) being synthesized and assayed (Table 2).

Substitutions at the phenyl ring were then investigated, using commercially available ethylbenzoyl acetates (Scheme 4). The only exception to this was **51** which was synthesized through the reduction of **50**. It was hoped that changes at the R^2 position with the [1,2,4]triazolo[1,5-*a*]pyrimidine derivatives, which had shown a notably increase in terms of ELISA activity, would be mirrored in the pyrazolo[1,5-*a*]pyrimidine. We proceeded to decorate the meta and para position of the phenyl ring with a variety of halides, in addition to CF_3, amine and nitro groups.

Of the three compounds that showed activity in the ELISA (**45**, **46**, and **50**) two showed acceptable E_{max} (**45** and **46**); however, all were progressed to the HR assay (Table 2). In the HR assay all three compounds showed an improved percentage of HR inhibition at 350 μM in comparison to **2**, with **45** and **46** maintaining a high level of activity at 20 μM (50 and 72 % respectively) (Table 3). Promisingly **46** maintained the same kinetic solubility as the original hit **2** (>250 μM), correcting the solubility issues that the series had previous suffered from (Table 2).

As the bromo group at the meta position appeared to be the best moiety on the phenyl ring it was kept as we sought to expand the molecule. This was attempted by initially chlorinating **46** at the C5 carbonyl, this was achieved in high yield by refluxing **46** in neat phosphorus oxychloride to yield **57**, followed by an SNAr of various amines to yield (**58**–**63**) (Scheme S6, Table S2). Additionally, a methoxy group was substituted in place on the carbonyl through reacting **46** with NaOH and MeOH to yield **64** (Scheme S6, Table S2). These additions were not tolerated due to solubility, further suggesting the vital nature of the NH group in the pyrazolo[1,5-*a*]pyrimidinecore (Table 2). Solubility could not be rescued, even using solubility handles such as carboxylic acids. Interestingly the solubility issues partially stemmed from the ELISA

Table 2
SAR results and kinetic solubility of **27**–**51**, **52**–**56** compared to hit **2**.

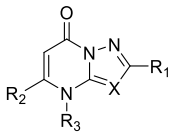

Compound	R^1	R^2	R^3	X	ELISA [a] (EC_{50} μM)	ELISA [a] (E_{max} %)	Solubility [b] (μM)
2	$-CF_3$	4-CH_3-C_6H_4	H	N	NA[c]	NA[c]	>250
27	$-CH_3$	-C_6H_5	H	N	NA[c]	NA[c]	242
28	$-CH_3$	4-F-C_6H_4	H	N	152	54	241
29	$-CH_3$	4-CF_3-C_6H_4	H	N	10.8 ± 1.3	64	>250
30	$-CH_3$	3-CH_3-C_6H_4	H	N	NA[c]	NA[c]	242
31	$-CH_3$	4-NO_2-C_6H_4	H	N	101.5 ± 10.5	64	>250
33	$-CF_3$	4-CH_3-C_6H_4	H	= CH-	55.5 ± 4.5	91	9
34	$-CH_3$	C_6H_5	H	= CH-	127	80	133
35	$-CH_3$	4-CH_3-C_6H_4	H	= CH-	139.0 ± 1.0	60	94
36	H	4-CH_3-C_6H_4	H	= CH-	120	91	164
37	Et	4-CH_3-C_6H_4	H	= CH-	79.5 ± 3.5	83	92
38		4-CH_3-C_6H_4	H	= CH-	190.0 ± 15.0	44	9
39		4-CH_3-C_6H_4	H	= CH-	n.e.[d]	n.e.[d]	5
40		4-CH_3-C_6H_4	H	= CH-	n.e.[d]	n.e.[d]	2
41		4-CH_3-C_6H_4	H	= CH-	n.e.[d]	n.e.[d]	5
42	$-CF_3$	4-CH_3-C_6H_4	$-CH_3$	= CH-	NA[c]	NA[c]	31
43	$-CF_3$	4-CH_3-C_6H_4	-Et	= CH-	251.0 ± 25.0	70	15
44	$-CF_3$	3-CH_3-C_6H_4	H	= CH-	NA[c]	NA[c]	34
45	$-CF_3$	4-Br-C_6H_4	H	= CH-	57.4 ± 5.3	53	117
46	$-CF_3$	3-Br-C_6H_4	H	= CH-	28.0 ± 3.0	73	>250
47	$-CF_3$	4-F-C_6H_4	H	= CH-	n.e.[d]	n.e.[d]	144
48	$-CF_3$	3-F-C_6H_4	H	= CH-	n.e.[d]	n.e.[d]	>250
49	$-CF_3$	3-CF_3-C_6H_4	H	= CH-	n.e.[d]	n.e.[d]	108
50	$-CF_3$	4-NO_2-C_6H_4	H	= CH-	194.4 ± 8.7	44	>250
51	$-CF_3$	4- NH_2–C_6H_4	H	= CH-	n.e.[d]	n.e.[d]	1
52	$-CF_3$	$-CH_3$	H	= CH-	181.5 ± 9.5	32	>250
53	$-CF_3$		H	= CH-	NA[c]	NA[c]	>250
54	$-CF_3$	$-CHF_2$	H	= CH-	35.3 ± 3.0	28	>250
55	$-CF_3$		H	= CH-	21.3 ± 2.8	36	>250
56	$-CF_3$	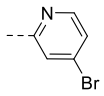	H	= CH-	50.4 ± 6.7	28	236

[a] Competitive ELISA assay using biotinylated BRC4 peptide to disrupt the RAD51-BRC4 interaction was performed according to the modified method described by Rajendra et al. [27]; CAM833, a known RAD51-BRCA2 disruptor developed by Scott et al. [15], was used as internal reference compound. E_{max}% refers to the percentage of the maximum activity at 100 μM of the tested compound and compared to the maximum activity of CAM833 at the same concentration.
[b] Kinetic solubility was performed in-house, as reported in the Experimental Section.
[c] NA = not active.
[d] n.e. = not evaluable due to poor solubility.

assay buffer, as a number of compounds were acceptable in the in-house kinetic solubility assay (Table S2). Regardless these compounds were not selected for further progression.

With modifications at the carbonyl group of the pyrazolo[1,5-*a*]pyrimidine core proving ultimately unsuccessful, one final attempt of optimizing **46** was attempted, looking to replace the phenyl group with either a heterocyclic moiety or an aliphatic group, increasing the explored chemical space around the scaffold through the synthesis of five compounds (**52**–**56**) (Scheme 5).

As can be seen in Table 2, small aliphatic modifications were generally not well tolerated with the methyl and cyclopropanyl group showing a loss in activity in the ELISA assay, suggesting the bulkier aromatic group is required. The other small aliphatic group in this series **54** maintained the EC_{50} value seen in **46** however with a reduced E_{max} which helps explains its poor performance in the HR assay (Table 3). Likewise, the introduction of a heterocyclic pyridine group was not well-tolerated, showing a poor E_{max} for both **55** and **56**.

The ability of compound **46** to bind RAD51 was tested through orthogonal biophysical assays both on the WT protein and on the isolated fully human monomeric unit [26,28]. MST experiments calculated the K_d of **46** as 12 μM for the binding to RAD51 WT and 55 μM for the binding to the RAD51 monomeric form (Fig. 3).

Table 3
Evaluation of HR inhibition.

Compound	HR 350 μM[a] (% inhib.)	HR 20 μM[a] (% inhib.)
2	65	–
29	19	–
31	NA[b]	NA[b]
33	79	NA[b]
34	40	–
35	n.e.[c]	n.e.[c]
36	82	6
37	82	NA[b]
45	84	50
46	95	72
50	88	2
52	NA[b]	NA[b]
54	27	–
55	n.e.[c]	n.e.[c]
56	40	–

[a] HR was evaluated by real-time PCR at two concentrations 350 μM and 20 μM (procedure described in the Experimental Section).
[b] NA = not active.
[c] n.e. = not evaluable due to poor solubility; '-' = the assay was not performed.

The binding of **46** to RAD51 WT was further corroborated by ^{19}F T_2 filter NMR experiments where the ^{19}F NMR signal of **46** (black) strongly decreased upon addition of RAD51 WT (red) (Fig. 4). The ^{19}F signal of the compound returned to its original intensity upon BRC4 addition (blue) confirming that the compound is displaced by the peptide in a similar manner to the parent compound **2**. The affinity of **46** for RAD51 WT and its monomeric form was also determined by NMR [30] confirming the previous results obtained by MST and ELISA (K_d of 38.8 μM ± 11.5 μM for RAD51 WT and a K_d of 99.6 ± 6.9 for the monomeric RAD51), with significant improvements achieved over the parent compound **2**.

Affinity data for **46**, obtained through orthogonal techniques were consistent and showed a slightly higher affinity of the compound for the oligomeric WT form in comparison to the monomeric form. Putting together these results, we selected **46** as the most promising hit for further biological evaluation.

2.4. Biological evaluation of 46

2.4.1. Characterization of HR inhibitory activity in cell-based assays

As a first experiment, HR-QA assay was carried out in a wide range of doses (1–400 μM) of **46;** the calculated IC_{50} value was 7.83 ± 3.19 μM (Fig. 5).

The HR-QA assay used for compounds' screening is a rapid tool which, in our experience, can give a reliable indication of HR efficiency in cells, in a relatively high-throughput manner [4]. A further HR inhibition study was performed by applying the m-Clover Lamin A assay (mCl-HR) [31,32]. This assay is based on the HR-dependent insertion of an mClover-containing sequence into a Cas-9-generated DSB in the LMNA gene. After the Cas-9 operated cleavage, the DNA DSB is repaired by HR with the mClover donor plasmid containing the homologous sequence, leading to the reconstitution of a fluorescent mClover-Lamin A fusion protein. This assay requires highly proliferating and transfection-permissive cells; therefore, it was performed on embryonal kidney cells (HEK-293) instead of BxPC-3 cells, which are characterized by a low transfection efficiency and a slow doubling time [33,34]. The transfection efficiency of HEK-293 cells was assessed by using a GFP-bearing plasmid and was found to be ≈ 45 %. (Fig. S3). Although in the HR-QA the lowest dose causing the highest degree of HR inhibition activity was found to be 30 μM, m-Clover-transfected HEK-293 cultures were treated with 50 μM **46**. This slightly increased dose was selected in consideration of the longer incubation time requested by the mCl-HR assay (3 days vs. the 5 h needed for HR-QA). As shown in Figure 6 , in the untreated m-Clover-transfected cultures (Ctr), approximately 20 % cells showed Lamin A fluorescence. Whereas treatment with **46** significantly reduced the number of Lamin A fluorescent cells to about 3.7 %. Notably, the HR inhibition level (≈80 %) was consistent with the results obtained in BxPC-3 cells by applying the HR-QA assay, highlighting the potential of **46** as a BRCA2-RAD51 inhibitor.

To confirm the results of the HR inhibition assays, we evaluated the reduction of RAD51 nuclear foci after the administration of DNA damaging agents, as it is an accepted parameter of compromised HR. In order to observe this, extensive DNA damage was induced in BxPC-3 cells by treating them with 50 μM cisplatin (CPL) for 1.5 h. The cells were subsequently treated for 5 h with 30 μM **46**. RAD51 nuclear foci were then detected by immunofluorescence. As shown in Fig. 7, treatment with **46** alone did not appear to cause DNA damage, since RAD51 foci were not evident in BxPC-3 cultures. On the contrary, as expected, the foci were visible in about 35 % cells of the CPL-treated cultures. However, upon administration of **46**, RAD51 foci were significantly reduced. These data are in good agreement with the results obtained in the HR experiments, and significantly supported the expected mechanism of action of the compound.

2.4.2. 46/TLZ combination studies in different BRCA2-proficient PDAC cell lines

The impairment of RAD51 functions caused by **46** is expected to increase the antineoplastic activity of PARPi [35,36]. This was verified in cell viability experiments, performed in three PDAC cell lines: HPAC, BxPC-3 and AsPC-1. HPAC and BxPC-3 are cell lines derived from a primary tumor, while the AsPC-1 line was isolated from the ascitic fluid of a PDAC metastasis [33,37–39]. The heatmap graph shows the differences between these cell lines in terms of expression of relevant genes for HR pathway (Fig. 8). In particular, BxPC-3 cells are characterized by a high level of RAD51, whose overexpression is linked to cell survival, drug resistance and poor patient prognosis [10,11]. These cells also show the highest level of TP53 expression. AsPC-1 cells carry different loss-of-function or missense mutations located in the DNA binding site of TP53, which leads to protein absence or impairment. Differently, HPAC is the only cell line showing the expression of wild-type TP53 [40,41]. In this aspect, HPAC cells represent an exception in the scenario of the PDACs commonly encountered in the clinical practice, since these cancer forms usually bear mutated TP53. However, we considered informative to include this model in our experiments for the purposes of our investigation.

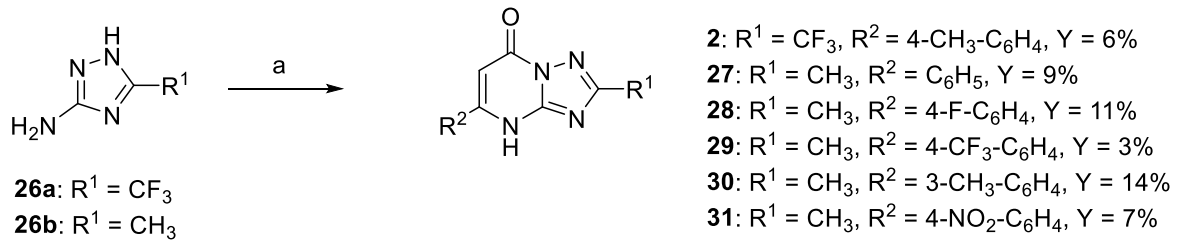

Scheme 1. Synthesis of initial series of **2** derivative [1,2,4]triazolo[1,5-*a*]pyrimidines. Reagents and conditions: (a) $R^2COCH_2COOCH_2CH_3$, acetic acid, reflux, 16 h, yields: 3–14 %.

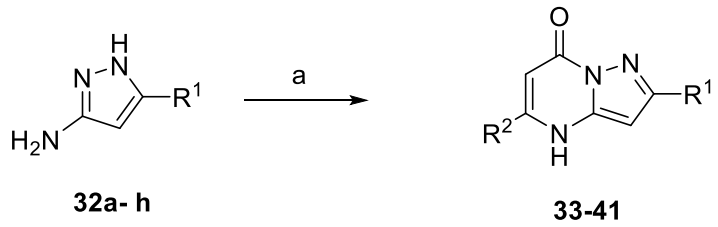

32a: $R^1 = CF_3$

32b: $R^1 = CH_3$

32c: $R^1 = H$

32d: $R^1 = CH_2CH_3$

32e: R^1 =

32f: R^1 =

32g: R^1 =

32h: R^1 =

33: $R^1 = CF_3$, R^2 = 4-CH_3-C_6H_4, Y = 23%

34: $R^1 = CH_3$, $R^2 = C_6H_5$, Y = 44%

35: $R^1 = CH_3$, R^2 = 4-CH_3-C_6H_4, Y = 50%

36: $R^1 = H$, R^2 = 4-CH_3-C_6H_4, Y = 14%

37: $R^1 = CH_2CH_3$, R^2 = 4-CH_3-C_6H_4, Y = 31%

38: R^1 = , R^2 = 4-CH_3-C_6H_4, Y = 39%

39: R^1 = , R^2 = 4-CH_3-C_6H_4, Y = 47%

40: R^1 = , R^2 = 4-CH_3-C_6H_4, Y = 36%

41: R^1 = , R^2 = 4-CH_3-C_6H_4, Y = 27%

Scheme 2. Initial scaffold hop and modifications at the R^1 position of the pyrazolo[1,5-*a*]pyrimidine **2** derivatives. Reagents and conditions: a) $R^2COCH_2COOCH_2CH_3$, acetic acid 120 °C MW, 16 h, yields: 14–50 %.

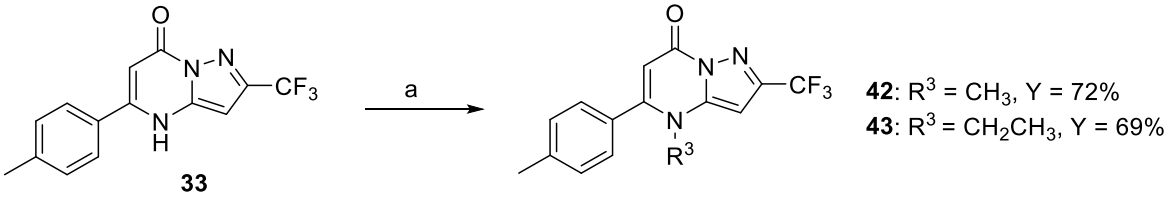

42: $R^3 = CH_3$, Y = 72%

43: $R^3 = CH_2CH_3$, Y = 69%

Scheme 3. Alkylation in the R^3 group. Reagents and conditions: (a) R^3I, K_2CO_3, Acetone, 35 °C, 3 h, yields 69–72 %.

The three selected PDAC cultures were used to study the antineoplastic effect of **46** in association with TLZ. TLZ is a PARPi approved by FDA on 2018 for the treatment of adults BRCA-mutated, HER2-negative, locally advanced or metastatic breast cancer [42]. Moreover, several studies are currently ongoing on pancreatic cancer [43–45]. Compared to other PARPi, TLZ exhibited a similar mechanism of action with an increased antineoplastic activity in vitro. In addition, TLZ was found to be about 100-fold more potent in trapping PARP1 [46–49]. The experiments performed in the selected PDAC cell lines were aimed at verifying whether **46** can significantly potentiate the effect of TLZ. In preliminary experiments, the three cell cultures were exposed for six days to scalar doses (0–5 μM) of TLZ, to evaluate the IC_{50} (Fig. S4). Since the calculated IC_{50} values resulted to be very similar among cell lines (1.8 μM for BxPC-3, 2.27 μM for HPAC and 2.66 μM for AsPC-1), the adopted dose for studying the combination effect with **46** was set at 2 μM TLZ for all the three cultures. **46** was administered at 30 and 50 μM, given singularly or in combination with TLZ for six days. This long exposure time was adopted since cell death is expected to be a consequence of progressive DNA damage accumulation, due to the simultaneous impairment of DNA SSBs and DSBs repair, caused by the PARPi and **46** respectively. In BxPC-3 cells, **46** alone caused a 25–30 % reduction of cell viability at both doses (Fig. 9), and this effect was increased by the addition of TLZ in a statically significant manner (≈60 %, with $p < 0.05$) (Fig. 9). This result is in complete agreement with the data of HR-QA (Fig. 5), which showed superimposable effects for the two doses of **46**, and also fits well with the mCl-HR experiment, shown in Fig. 6. The **46**/TLZ combination had a similar statistically significant effect in HPAC cells. Whereas in AsPC-1 this effect appeared to be less marked, but was still statistically significant at 50 μM. A possible explanation for this can be provided by the heatmap in Fig. 8. Indeed, AsPC-1 cells are characterized by the lowest BRCA2 expression, compared to BxPC-3 and HPAC, while the expression level of RAD52 is more than 2-fold higher than BRCA2. For these characteristics, it can be hypothesized that in AsPC-1 cells alternative HR, such as the RAD52-mediated HR, which is

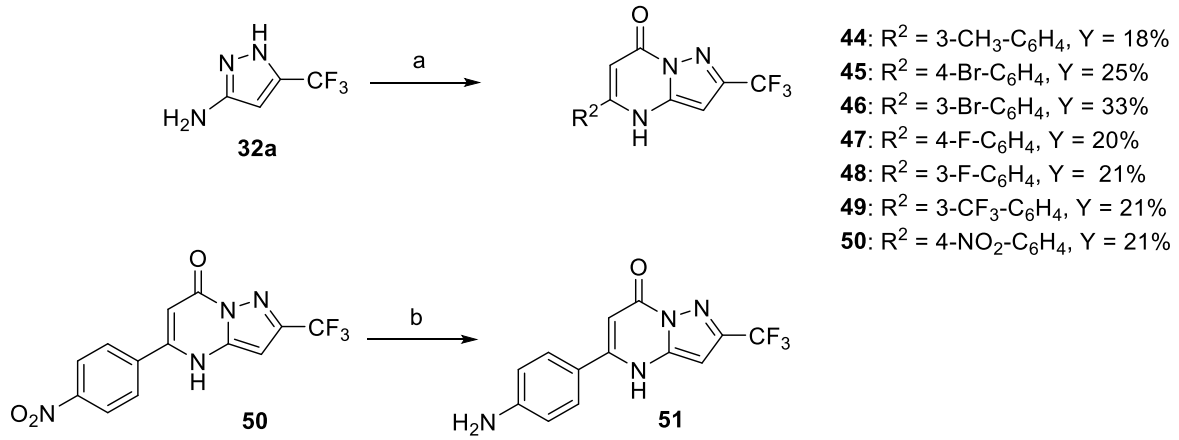

Scheme 4. Modifications at the R^2 position of the pyrazolo[1,5-*a*]pyrimidine **2** derivatives. Reagents and conditions: (a) $R^2COCH_2COOCH_2CH_3$, acetic acid 120 °C MW, 16 h, yields: 18–33 % (b) $Pd(OH)_2/C$, HCO_2NH_4, MeOH, reflux, 30 min, yield: 99 %.

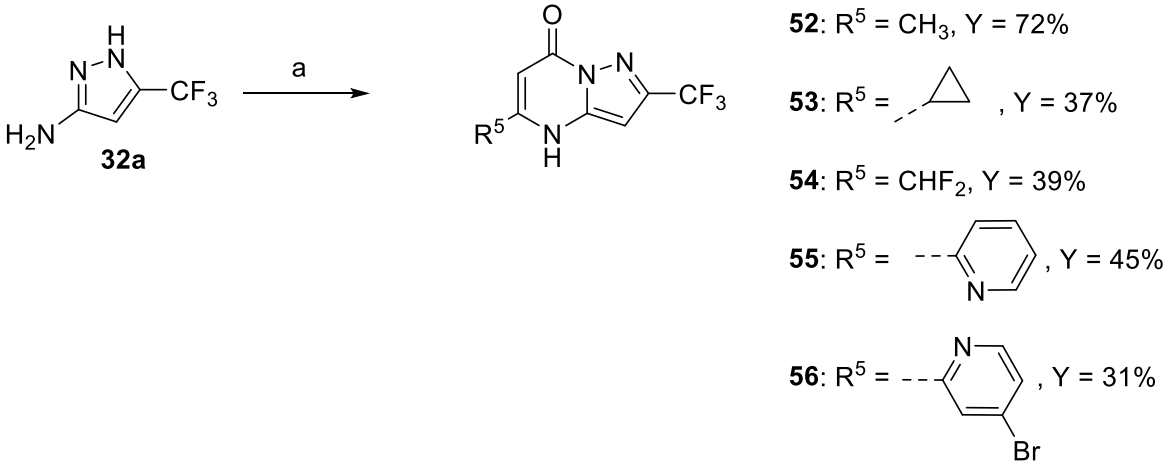

Scheme 5. Modifications at the R^5 position of the pyrazolo[1,5-*a*]pyrimidine **2** derivatives. Reagents and conditions: (a) $R^5COCH_2COOCH_3/R^5COCH_2COOCH_2CH_3$, Acetic acid, 120 °C MW, 16 h, yields: 31–72 %.

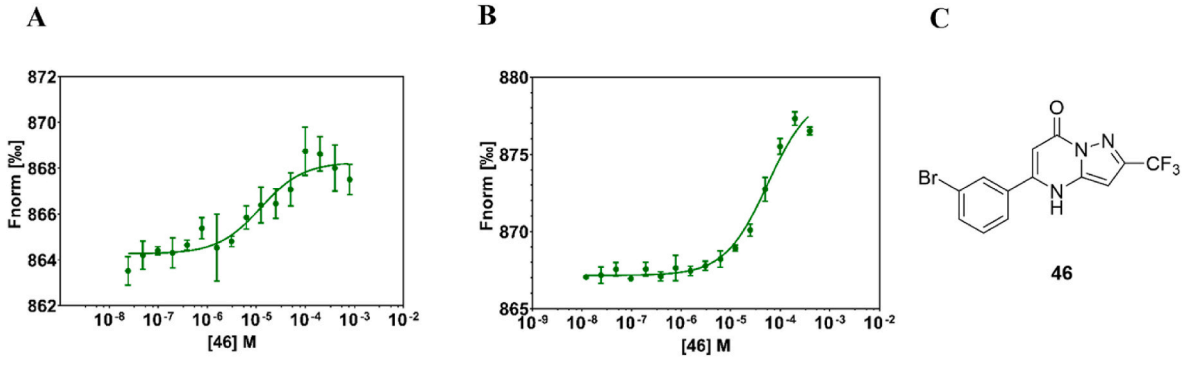

Fig. 3. MST analysis of **46** binding RAD51 WT (A) or RAD51 [F86E, A89E] (B). Both proteins were labeled with RED-tris-NTA 2nd Generation and tested at a final concentration of 10 nM. The presented data are the average of three replicates. C) Structure of **46**.

independent from BRCA2, might prevail, thus explaining the compromised efficacy of BRCA2-RAD51 inhibitors [50,51].

Subsequently, we evaluated whether the results shown in Fig. 9 could be explained by the involvement of cell death, which is the desired goal of antineoplastic treatments [52]. Due to the reduced efficacy observed in AsPC-1 cultures, the experiment was performed only in HPAC and BxPC-3 cells. Cells were treated with the **46**/TLZ combination for six days, in the presence of 20 μM Z-VAD-FMK (a well-known pan-caspase inhibitor) or 20 μM to the Necrostatin-1 (Nec-1, a necroptosis inhibitor) [53,54]. **46** was administered at 30 μM, the lowest dose causing statistically significant effects in the cell viability experiments (Fig. 9). In cultures treated with the **46**/TLZ combination, the administration of Z-VAD-FMK resulted in significantly increased cell viability (Fig. 10 A). On the contrary, administration of Nec-1, did not

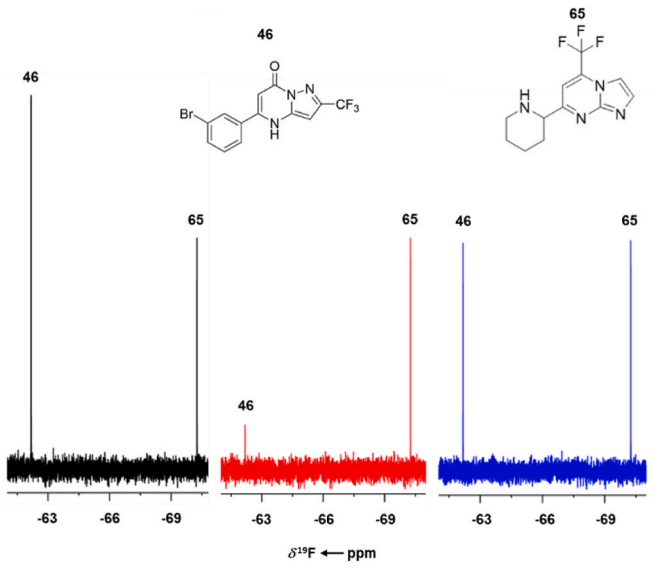

Fig. 4. ^{19}F T_2 filter NMR experiments of 20 μM **46** and 20 μM **65** (negative reference, identified from preliminary screening) in the absence (black) and in presence of 0.5 μM RAD51 WT (red) or 0.5 μM RAD51 WT + 5 μM BRC4 (blue). The ^{19}F T_2 signal of **46** strongly decreased in the presence of RAD51 WT as a consequence of the line broadening of its ^{19}F NMR signal due to the binding event. The sharpening of the **46** ^{19}F signal, observed upon addition of BRC4, was due to its displacement from RAD51 WT by the peptide. No change of the ^{19}F- signals of fragment **65** (negative control) was observed.

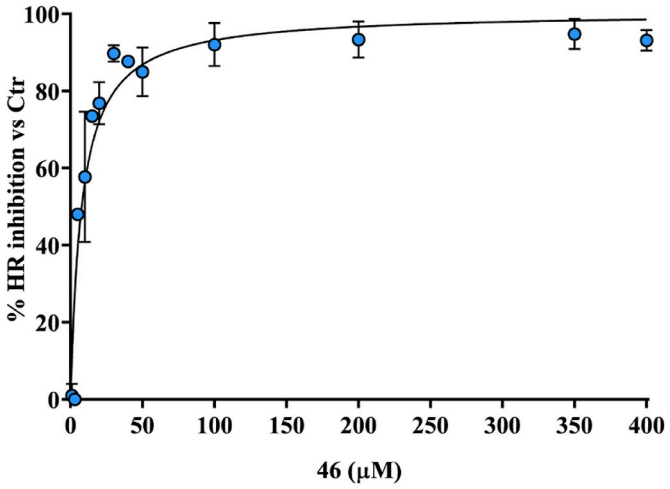

Fig. 5. HR inhibition caused by increasing doses of **46** administered to BxPC-3 cells during 5 h of plasmid transfection. HR was evaluated by real-time PCR, as described in the Experimental Methods section. A plateau effect was observed for doses higher than 30 μM, with no statistically significant difference in the HR inhibitory power caused by **46**, measured in the dose range 30–400 μM (assessed by ANOVA). To extrapolate the IC_{50} value, data were analyzed by applying the least squares regression fit; the theoretical regression curve (R^2 = 0.91) is shown in the graph.

affect the antiproliferative effect of the **46**/TLZ combination (Fig. 10 B). These results confirmed the involvement of apoptosis, reproducing the desired mechanism of SL triggered by the combination between RAD51-BRCA2 and PARP inhibitors.

In order to explore the selectivity of the **46**/TLZ combination for cancer cells, we analyzed the toxicity of the combination on normal epithelial cells isolated from human pancreas (H-6037). H-6037 cells were treated with 30 μM **46** alone or in combination with 2 μM TLZ for six days. As shown in Fig. 11, administration of TLZ did not affect H-6037 cell viability, and **46** only caused a weak, ≤20 % inhibition. Notably, these effects were lower than those observed in the cancer models (Fig. 9). Moreover, in H-6037 cultures, the administration of **46** was unable to increase the antiproliferative effects of TLZ, since no statistically significant difference was observed between the cells exposed to **46** and those receiving the combination treatment. Although preliminary, these results are in line with the idea that a combined inhibition of PARP and BRCA2-RAD51 function should preferentially affect cancer cells.

*2.4.3. Evaluation of **46**/TLZ combination effect in PDAC 3D models*

Commonly used monolayer 2D cultures cannot fully represent the original tumor histology. On the contrary, 3D models exhibit remarkable similarities to *in vivo* tumor architecture and for this feature they are important tool in drug development [55,56]. For this reason, the antiproliferative effect caused by the combination of 50 μM **46** with 2 μM of TLZ was also evaluated in two different PDAC organoids: PT291 and PDM41, characterized by adenocarcinoma, cholangiocarcinoma, and adenocarcinoma ductal type histology, respectively. The effect of the combination **46**/TLZ was evaluated after a six-day treatment and the obtained results are shown in Fig. 12. The combination treatment significantly increased the effects of TLZ in both organoid models, reinforcing the results obtained in 2D cellular assays. In particular, the advantage of the drug combination was evident in PT291, in which the co-administration with **46** caused a 50 % reduction of cell viability, compared to the single TLZ treatment.

Since in 2D cellular assays treatment with **46** resulted in impaired HR repair pathway, its combination with PARPi TLZ should lead to increased DNA damage. Therefore, in the PT291 organoid we evaluated the level of DNA damage following treatment with **46**/TLZ by using an immunofluorescent assay for the detection of γ-H2AX foci, a recognized DNA damage marker (Fig. 13).

Interestingly, when given as single treatments, both **46** and TLZ did not cause significant γ-H2AX labeling, compared to the untreated PT291. In contrast, the combination of the two compounds resulted in a statistically significant, 3-fold increase of DNA damage signatures, confirming the results of the viability experiment (Fig. 12). This result agrees with the postulated mechanism of action of the two compounds, which are expected to significantly compromise DNA integrity as a result of their combined action. Moreover, it further corroborates all the data obtained in the previously described experiments.

Overall, the data obtained in 2D and 3D pancreatic cancer models agree with each other and support our recently proposed anticancer drug discovery concept, dubbed 'fully small-molecules-induced SL'.

3. Conclusions

SL represents a promising avenue for medicinal chemistry in the pursuit of anticancer therapies, as the reliance of several tumors on specific DDR mechanisms induces a level of vulnerability. In this context, our strategy is based on the combination between BRCA2-RAD51 small molecule inhibitors and PARPi, in order to simultaneously impair two different DNA repair pathways to induce SL. Building upon the group's previous works in designing RAD51-BRCA2 inhibitors, we leveraged for the first time a ^{19}F NMR fragment screening on the oligomeric RAD51 form and identified two suitable hits, **2** and **3**. Subsequently, several rounds of synthetic optimization, guided by ELISA, culminated in the identification of **46**. The compound proved to inhibit BRCA2-RAD51 interaction in the low micromolar range and, importantly, induced SL as result of the combination with PARPi TLZ in pancreatic cancer cells. Notably, the use of pancreatic cancer cells with different gene expression patterns, the optimization of an additional HR assay, and the employment of 3D cell cultures allowed a more comprehensive characterization of the mechanism-of-action and the combination effect with PARPi of **46**.

This work adds credence to the SL paradigm for tackling oncological

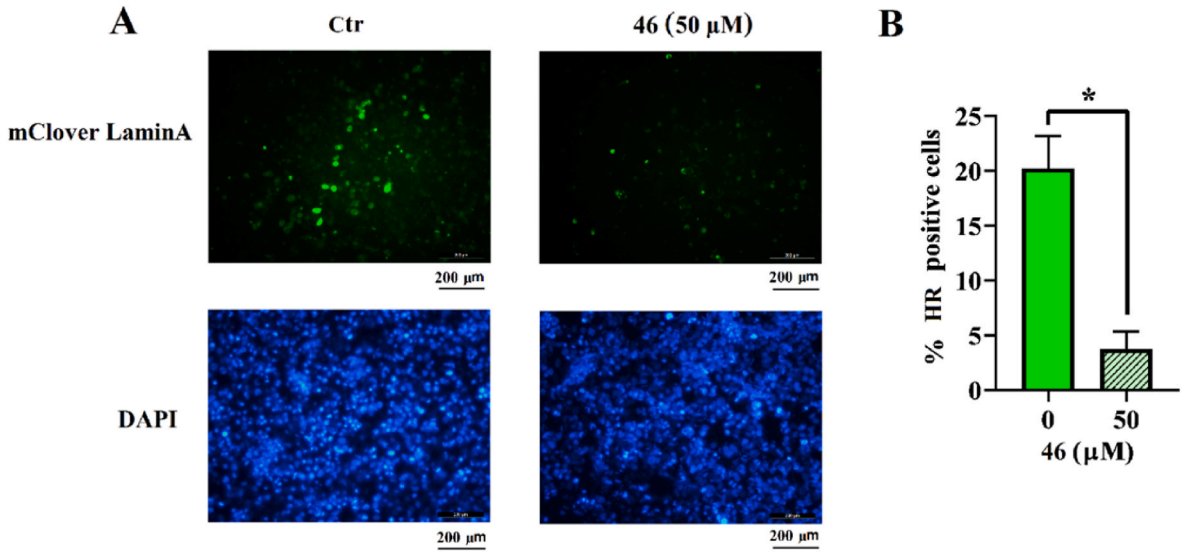

Fig. 6. A) Representative microscopic fields showing fluorescence of HEK-293 transfected with the assay plasmids (Lamin A-targeting sgRNA-spCas9 and mClover Lamin A donor). **46** (50 μM) administration led to a remarkable decrease in HR positive cells, compared to the Ctr. The blue fluorescence shows DAPI-stained DNA. Scale bar, 200 μm. B) The graph shows the percentage of HR-proficient cells in untreated and **46** (50 μM) exposed samples, highlighting a statistically significant decrease (*p = 0.0199) due to the treatment. Approximately 200 cells per sample were analyzed in two independent experiments, and the fluorescence intensity was measured by using the ImageJ software. Statistical significance was assessed by Student's t-test.

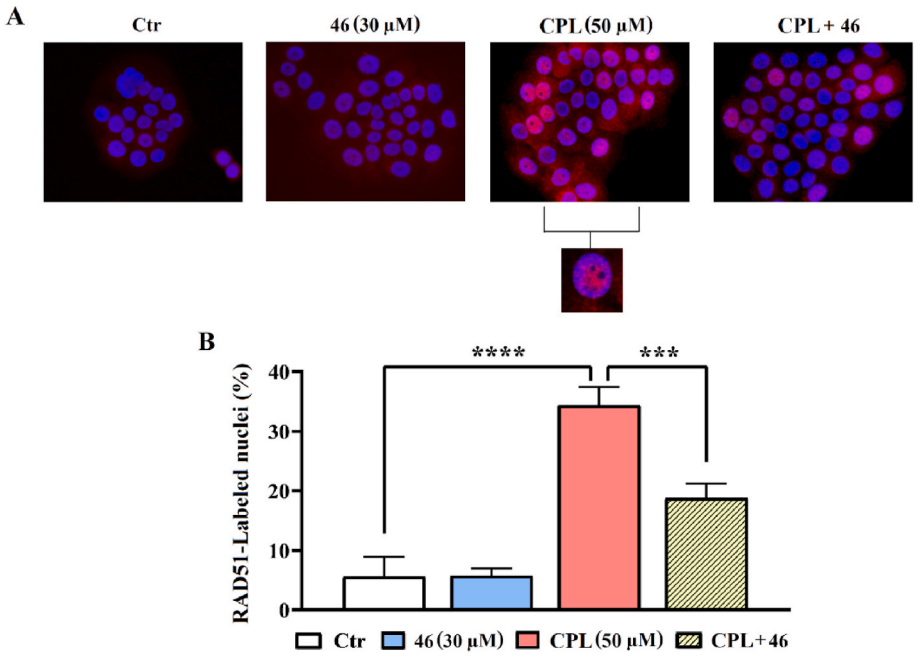

Fig. 7. A) Representative pictures showing DAPI stained BxPC-3 cell nuclei merged with the corresponding RAD51-labeling. A higher magnification detail of RAD51 nuclear foci was included for the CPL-exposed culture. B) The bar graph shows the percentage of labeled assessed in the cell cultures. In CPL-exposed cultures, RAD51 labeling was detected in 35 % nuclei (****p < 0.0001, compared to Ctr); in cells exposed to both **46** and CPL only 18 % cell nuclei showed RAD51 labeling, a statistically significant reduction compared to CPL-exposed cells (***p = 0.0004). RAD51-labeled nuclei were assessed by two independent observers who analyzed the treated cultures, counting approximately 200 cells for each treatment sample. Data were statistically evaluated by applying the one-way ANOVA test.

unmet needs such as pancreatic cancer. We believe that **46** can serve as a useful tool for further investigation of the RAD51 SL mechanism, as well as a starting point for further drug discovery campaigns.

4. Experimental section

4.1. Protein expression

The 6 × His tag RAD51 WT and the 6 × His tag monomeric RAD51 [F86E, A89E] were purified as already reported by Schipani et al. [26] and Rinaldi et al. [28], respectively.

4.2. Biophysical experiments

4.2.1. NMR (fragment analysis)

All the spectra were recorded at 298 K using a Bruker FT-NMR 600 MHz ADVANCE NEO equipped with a Cryoprobe QCI $^{1}H/^{19}F–^{13}C/^{15}N$ – D and a Samplejet™ autosampler with temperature control. For all

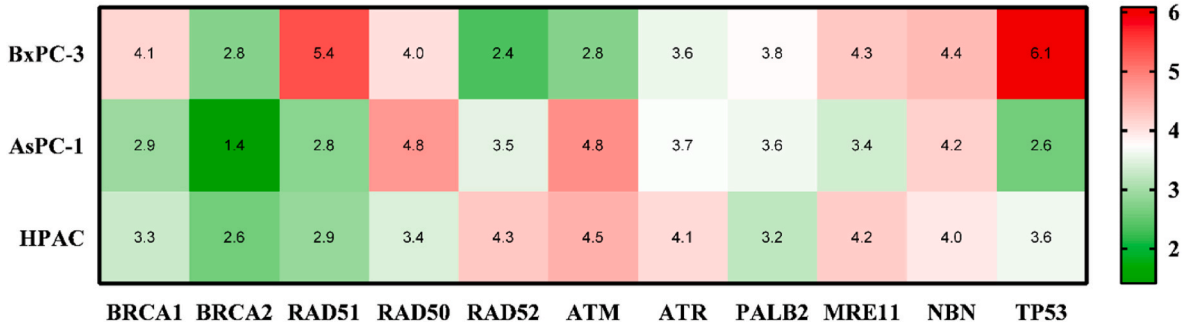

Fig. 8. Heatmap obtained using Depmap, the Cancer Dependency Map portal (https://depmap.org/portal/); as reported in Depmap, relative gene expression values are inferred from RNA-seq data using the RSEM tool and are reported after log2 transformation, using a pseudo-count of 1; log2(TPM+1). It shows the gene expression profile of the main HR genes (indicated at the bottom of the graph) in the three PDAC cell lines used (indicated at the left of the graph). The reported colors are referred to the scale on the right: the more intense the red, the more expressed the gene; otherwise, the more intense the green, the less expressed the gene.

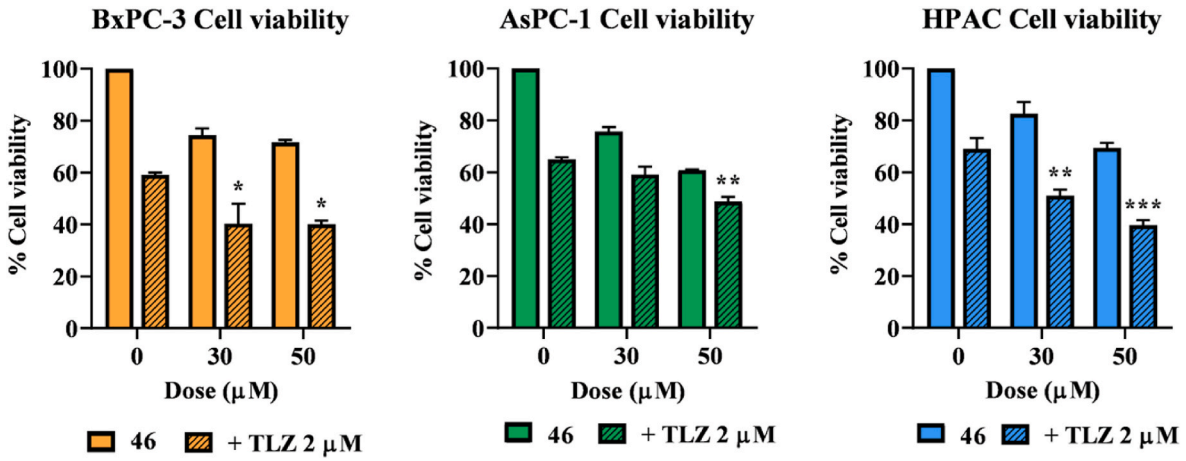

Fig. 9. Antiproliferative effect caused by 30 and 50 μM **46**, administered singularly or in combination with 2 μM TLZ, measured in BxPC-3, AsPC-1 and HPAC cells after six days of treatment. In BxPC-3 and HPAC cells, TLZ + **46** markedly reduced cell viability, with a statistically significant effect compared to TLZ alone (*$p < 0.05$; **$p < 0.005$; ***$p = 0.0001$). In AsPC-1 cells, the efficacy of the compounds' association was less marked, compared to TLZ effect; however, a statistically significant difference was observed for the association TLZ +50 μM **46** (**$p < 0.005$). Data were statistically analyzed using the two-way ANOVA followed by Tukey's multiple comparisons test, to evaluate the differences between the effects caused by the compounds' combination vs those caused by the single TLZ treatment.

compounds, 1D ^{1}H NMR spectra were recorded (ns 256, d1 5s, sw 16 ppm, aq 2.5 s, mixing time 10 ms) in the protein storage buffer, the water suppression was obtained with the excitation sculpting sequence. ^{19}F T_2 filter experiments were recorded using CPMG spin-echo scheme with a 50 ms time interval between the 180 pulses, total length 200 ms, 64 scans, sw 60 ppm, aq 0.96s and d1 5 s. The data were multiplied by an exponential window function with 1 Hz line broadening prior to Fourier transformation.

The experiments were performed in buffer 20 mM HEPES pH 8, 250 mM KCl. 2 mM DTT, 100 μM EDTA, 1 % Glycerol, 10 % D_2O for the lock signal, and a DMSO-d_6 final concentration of 1 %. For binding experiments the concentration of the compounds (mixture or single) and RAD51 WT were 40 μM and 1 μM, respectively. In the displacement experiments, the concentration BRC4 was 20 μM.

K_D measurements:

The K_D values were measured by the Dalvit et al. [22–24,30] method using only two concentrations of the ligand (L_0 and L) and the following expression:

$$K_D = \frac{\left\{(R_2)_{+E+L_0} - (R_2)_{-E+L_0}\right\}[L_0] - \left\{(R_2)_{+E+L} - (R_2)_{-E+L_0}\right\}[L]}{\left\{(R_2)_{+E+L} - (R_2)_{+E+L_0}\right\}}$$

were $(R_2)_{-E+L_0}$ is the transverse relaxation rate of the compound at the initial concentration in the absence of protein, $(R_2)_{+E+L_0}$ in presence of protein and $(R_2)_{+E+L}$ is the transverse relaxation rate of the compound at the second concentration in presence of protein. The experiments were performed in duplicates for both WT and monomeric RAD51 forms.

For RAD51 WT, **46** was analyzed by ^{19}F T_2 filter experiments at 10 μM (L_0) in the absence and in presence of 0.5 μM RAD51 WT using 64 scans, sw 20 ppm, aq 0.72s, d1 5 s and different total spin echo lengths (1, 92, 184, 368 and 736 ms). Two successive compound additions brought the final compound concentration to 60 and 160 μM, respectively.

The K_D of **46** binding to monomeric RAD51 was obtained recording the same ^{19}F T_2 filter experiments performed on the WT sample, with the same compound concentrations (10, 60 and 160 μM) and 1 μM of protein in the following buffer 20 mM HEPES pH 8, 100 mM Na_2SO_4. 2 mM DTT, 100 μM EDTA, 1 % Glycerol, 10 % D_2O.

Negative controls (**1**, and **65**) were identified in the initial screening as non-binder compounds.

4.2.2. Microscale thermophoresis

RAD51 WT and RAD51 [F86E, A89E] were labeled with His-Tag Labeling Kit RED-tris-NTA 2nd Generation (NanoTemper Technologies, München, Germany), which specifically binds to the His-tag of proteins. According to manufacturer instruction, 100 μL of 100 nM dye solution in labelling buffer were prepared and mixed with 100 μL of 200 nM RAD51 WT or RAD51 [F86E, A89E] sample and incubated for 30

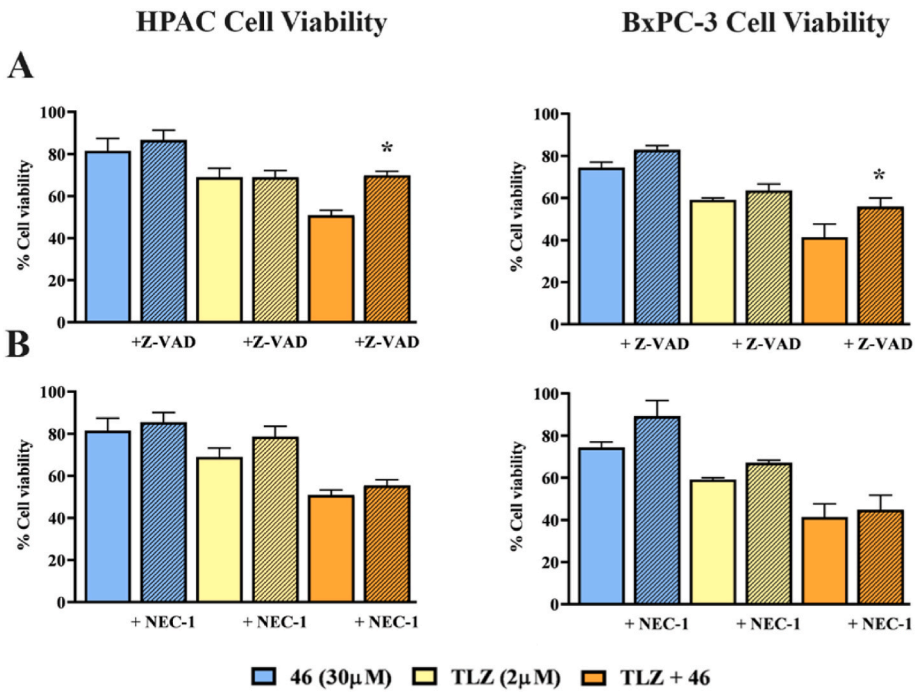

Fig. 10. Evidence of cell death pathways following the **46**/TLZ treatment in HPAC (left) and BxPC-3 (right) cells. **A.** Involvement of apoptosis. Cells were treated for six days with 30 μM **46**, given singularly or in combination with 2 μM TLZ. 20 μM Z-VAD-FMK was added mid-treatment and then every 24 h. Data were statistically analyzed using two-way ANOVA followed by Tukey's multiple comparisons test (*$p < 0.05$, compared to the culture treated with **46**/TLZ). **B.** Involvement of necroptosis. Cells were treated for six days with 30 μM **46,** singularly or in combination with 2 μM TLZ. 20 μM Nec-1 was added mid-treatment and then every 24 h. Data were statistically analyzed using two-way ANOVA followed by Tukey's multiple comparisons test. No evidence of necroptosis was observed.

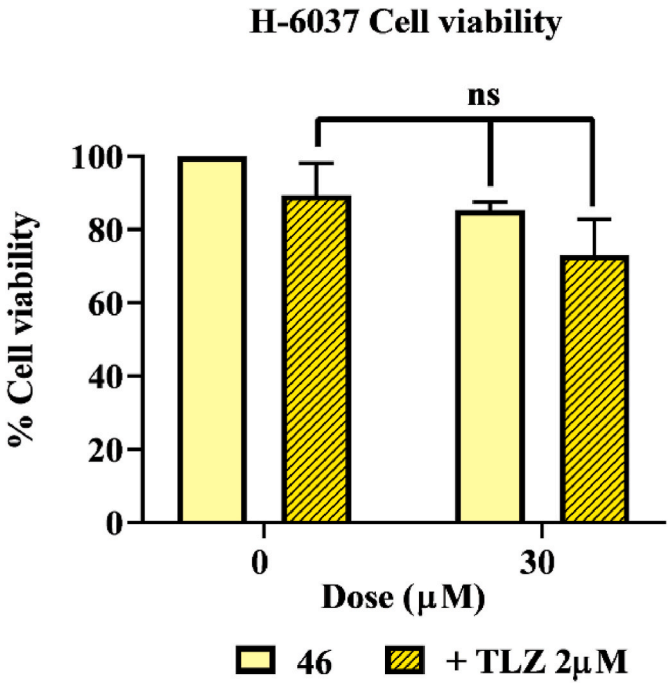

Fig. 11. H-6037 cell viability measured after six days exposure to 30 μM **46** and 2 μM TLZ, given alone or in combination. Data were statistically analyzed by two-way ANOVA followed by Tukey's multiple comparisons test. 30 μM **46** caused a ≈20 % inhibition of H-6037 cell viability ($p < 0.05$). No statistically significant difference was observed when the effect of the **46**/TLZ combination was compared with those caused by the two compounds administered as single treatments; ns = not significant.

min at room temperature in the dark. Samples were then centrifuged for 10 min at 4 °C at maximum speed. MST measurements were performed at 20 % excitation and high power on 16 premium capillaries (Nano-Temper Technologies, München, Germany). 10 nM of labeled proteins (RAD51 WT or RAD51 [F86E, A89E]) were tested against 16 different concentrations of the **46** previously dissolved in 100 % DMSO and then diluted in buffer to a final 5 % DMSO concentration in each sample. The highest **46** concentration tested was 800 μM for experiments carried out with RAD51 WT and 400 μM for experiments with monomeric RAD51. 3 independent binding curves were fitted using the Affinity Analysis software of Nanotemper Technologies and analyzed at 2.5 s to obtain binding affinity data. Results were then re-graphed using GraphPad Prism 9. RAD51 WT was labeled in a buffer containing Hepes pH 8.00 20mM, KCl 250 mM, EDTA 0.1 mM, Glycerol 5 % and assays were performed diluting the protein with a buffer containing Hepes pH 8.00, 20 mM, KCl 250 mM, EDTA 0.1 mM, Glycerol 5 % supplemented with Tween 20 0.05 % v/v, PEG8000 0.1 % w/v, Sodium Deoxycholate 0.5 mM. RAD51 monomer was labeled in a buffer containing Hepes pH 8.00 20 mM, Na_2SO_4 100 mM, EDTA 0.1 mM, Glycerol 5 % and assays were performed diluting the protein with a buffer containing Hepes pH 8.00 20 mM, Na_2SO_4 100 mM, EDTA 0.1 mM, Glycerol 5 % supplemented with Tween 20 0.05 % v/v, PEG8000 0.1 % w/v, Sodium Deoxycholate 0.5 mM.

4.3. Chemistry

4.3.1. Materials and methods

Solvents and reagents were obtained from commercial suppliers and used without further purification. NMR experiments were run on a Bruker Avance III 400 MHz spectrometer (400.13 MHz for 1H and 100.62 MHz for 13C), equipped with a BBI probe and Z-gradients, or on a Bruker FT NMR Avance III 600-MHz spectrometer (600.130 MHz for 1H and 150.903 MHz for 13C) equipped with a 5 mm CryoProbe QCI quadruple resonance, a shielded Z-gradient coil, and the automatic

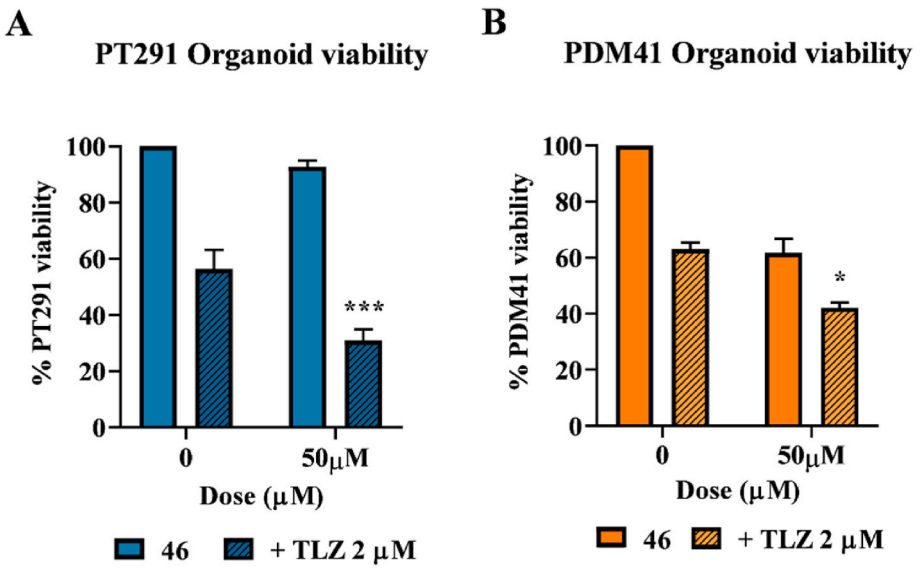

Fig. 12. Antiproliferative effect caused by **46** administered singularly or in combination with 2 μM TLZ and evaluated in two different 3D models of PDAC: the PT291 (A) and the PDM41 (B). (A) The six days co-administration of the two compounds led to a marked decrease in organoids' viability, strongly potentiating the anti-proliferative effect of TLZ. The two-way ANOVA test, followed by Tukey's multiple comparisons test, indicated a statistically significant difference produced by the coadministration compared to the single TLZ treatment (***p = 0.0003). (B) In PDM41 PDAC organoid culture the compounds' association showed a less remarkable, but statistically significant effect (*p = 0.0116, compared the single TLZ treatment).

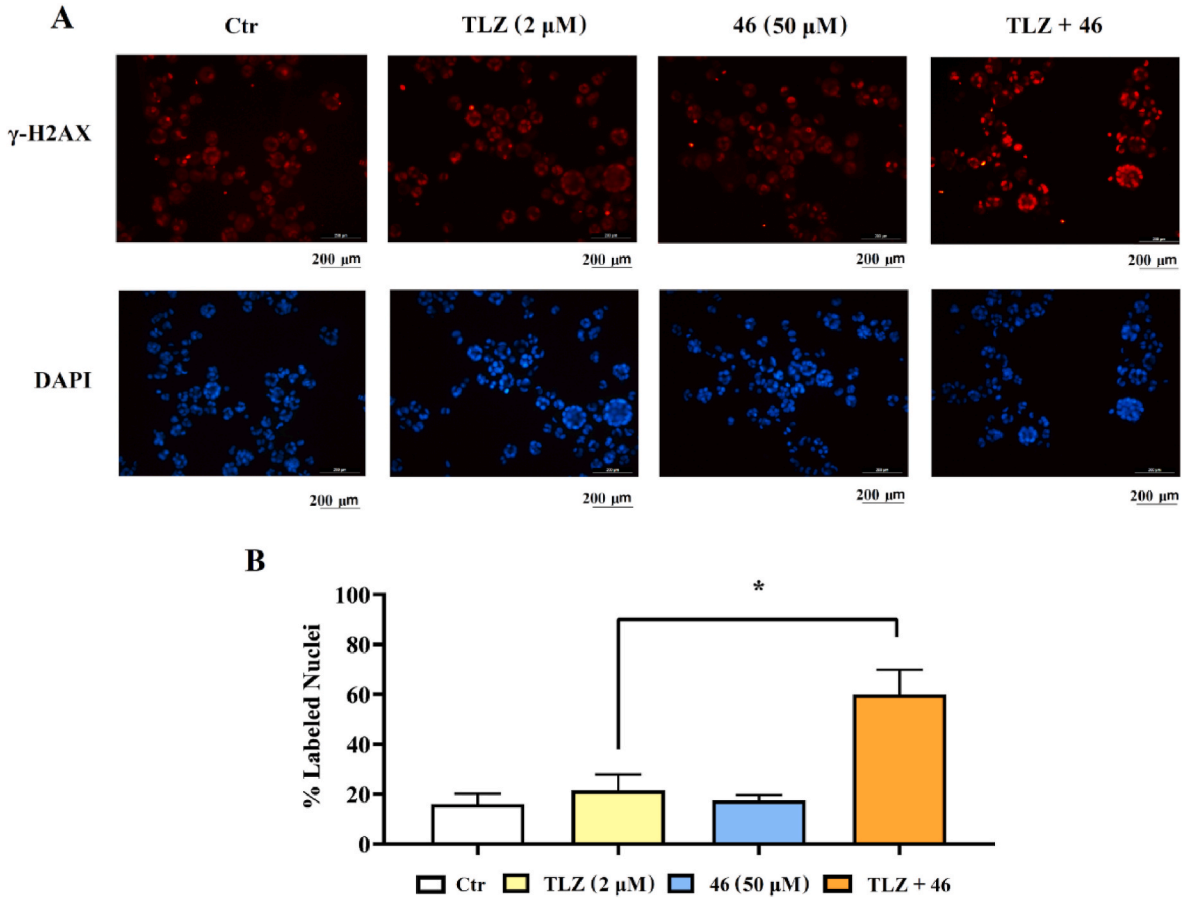

Fig. 13. Evaluation of DNA damage in the PT291 organoid culture treated for 24 h with 2 μM TLZ and 50 μM **46**, given singularly or in combination. (A) Representative pictures showing DAPI-stained cell nuclei and the corresponding immune-labeling of γ-H2AX, a marker of DNA damage. In PT291, the coadministration of **46** and TLZ led to increased γ-H2AX labeling. (B) The bar graph shows the percentage of γ-H2AX labeled nuclei, assessed with the aid of ImageJ software. The statistical analysis was carried out by applying one-way ANOVA followed by Tukey's multiple comparisons test; a statistically significant difference was found between the organoid culture treated with TLZ alone and that exposed to the compounds' combination. *p = 0.0127.

sample changer SampleJet NMR system. Spectra were acquired at 300 K, using deuterated dimethylsulfoxide (DMSO-d_6) or deuterated chloroform ($CDCl_3$-*d*)as a solvent. Chemical shifts for 1H and 13C spectra were recorded in parts per million using the residual nondeuterated solvent as the internal standard.The coupling constants of the splitting patterns were reported in Hz and were indicated according i.e. as singlet (s), doublet (d), triplet (t) etc or multiplet (m). UPLC−MS analyses were run on a Waters ACQUITY UPLC/MS system consisting of an SQD (single quadrupole detector) mass spectrometer equipped with an electrospray ionization interface and a photodiode array detector. The PDA range was 210–400 nm. The analyses were performed on either an ACQUITY UPLC HSS T3 C18 column (50 × 2.1 mm i.d., particle size 1.8 μm) with a VanGuard HSS T3 C18 precolumn (5 mm × 2.1 mm i.d., particle size 1.8 μm) (logD <1) or an ACQUITY UPLC BEH C18 column (50 mm × 2.1 mm i.d., particle size 1.7 μm) with a VanGuard BEH C18 precolumn (5 mm × 2.1 mm i.d., particle size 1.7 μm) (log D > 1). The mobile phase was 10 mM NH4OAc in H2O at pH 5 adjusted with AcOH (A) and 10 mM NH4OAc in MeCN–H2O (95:5) at pH 5 (B). Electrospray ionization in positive and negative mode was applied in the mass scan range 100–500 Da. Methods and gradients used were the following: Generic method. Column: Waters ACQUITY UPLC BEH C18, 1.7 μm, 50 mm × 2.1 mm i.d. Linear gradient: 0−0.2 min, 5 % B; 0.2−2.7 min, 5−95 % B; 2.7−2.8 min, 95−100 % B; 2.8−3.0 min, 100 % B. Flow rate: 0.5 mL/min. Apolar method. Column: Waters ACQUITY UPLC BEH C18, 1.7 μm, 50 mm × 2.1 mm i.d. Precolumn: VanGuard BEH C18, 1.7 μm, 5 mm × 2.1 mm i.d. Gradient: 0−0.2 min, 50 % B; 0.2− 2.7 min, 50−100 % B; 2.7−3.0 min, 100 % B. Flow rate: 0.5 mL/min. Compounds were named according to IUPAC convention. All final compounds displayed ≥95 % purity as determined by UPLC/MS analysis.

4.3.2. Preparation of derivatives **2, 27–51, 60– 64**

4.3.2.1. General procedure 1. Under nitrogen 3-amino-5-trifluoromethyl-4*H*-1,2,4-triazole (1 equiv) or 3-amino-5-methyl-4*H*-1,2,4-triazole (1 equiv) was dissolved in acetic acid (1.5 mL). The appropriate ethyl benzoyl acetate was then added (1.2 equiv) and the reaction was then heated with stirring under reflux for 16 h. Upon cooling the resulting white precipitate was filtered and rinsed with diethyl ether (1.5 mL) to yield the title compound.

4.3.2.2. General procedure 2. Under nitrogen the appropriate aminopyrazole (1 equiv) was dissolved in acetic acid (1.5 mL). The appropriate ethyl benzoyl acetate was then added (1.2 equiv) and the reaction was then heated with stirring with microwave radiation at 120 °C for 16 h. Upon cooling the resulting white precipitate was filtered and rinsed with diethyl ether (1.5 mL) to yield the title compound.

4.3.2.3. General procedure 3. Under nitrogen, to a suspension of 5-(*p*-tolyl)-25-(*p*-tolyl)-2-(trifluoromethyl)-4*H*-pyrazolo[1,5-*a*]pyrimidin-7-one (1 equiv) and K_2CO_3 (4 equiv) in dry acetone (2 mL) was added excess of the appropriate alkyl iodide (10 eq) in one portion at room temperature. The reaction mixture was heated at 35 °C for 3 h. The reaction crude was partitioned between DCM (50 mL) and $NaHCO_3$ saturated solution (50 mL), the aqueous layer was washed with DCM (2 × 10 mL) and the combined organic layers were dried over Na_2SO_4, concentrated to dryness *in vacuo* to yield the title compound.

4.3.2.4. 5-(p-tolyl)-2-(trifluoromethyl)-4H-[1,2,4]triazolo[1,5-a]pyrimidin-7-one (2). The title compound was synthesized following the general procedure 1 with 3-amino-5-trifluoromethyl-4*H*-1,2,4-triazole (250 mg, 1.64 mmol) and 3-oxo-3-*p*-tolyl-propionic acid ethyl ester (0.36 mL, 1.8 mmol) to yield the title compound as an off-white solid (27 mg, yield 6 %). ^{1}H NMR (400 MHz, DMSO-d_6) δ 7.79 (d, J = 8.1 Hz, 2H), 7.39 (d, J = 8.0 Hz, 2H), 6.42 (s, 1H), 2.40 (s, 3H). ^{13}C NMR (125 MHz, DMSO-d_6) δ 155.55 (q), 152.22 (J = 39 Hz, -*C*-CF_3), 152.13 (J = 26 Hz, -*C*-C-CF_3), 141.78 (q), 129.65 (2 X CH), 128.62 (C), 127.57 (2 X CH), 119.04 (J = 271 Hz, -*C*F_3), 97.74 (CH), 20.95 (CH_3). t_R 1.45 min (generic method). ESI-MS for $C_{13}H_9F_3N_4O$: calculated 294.07, found *m/z* 293.1 M − and 295.0 M+.

4.3.2.5. 2-methyl-5-phenyl-4H-[1,2,4]triazolo[1,5-a]pyrimidin-7-one (27). The title compound was synthesized following the general procedure 1 with 3-amino-5-methyl-4*H*-1,2,4-triazole (138 mg, 1.41 mmol) and ethyl benzoylacetate (0.27 mL, 1.56 mmol) to yield the title compound as an off-white solid (27 mg, yield 9 %). ^{1}H NMR (400 MHz, DMSO-d_6) δ 7.94 (dd, J = 6.8, 3.0 Hz, 2H), 7.58–7.43 (m, 3H), 6.36 (s, 1H), 2.41 (d, J = 1.5 Hz, 3H). t_R 1.20 min (generic method). ESI-MS for $C_{12}H_{10}N_4O$: calculated 226.09, found *m/z* 225.1 M − and 227.0 M+.

4.3.2.6. 5-(4-fluorophenyl)-2-methyl-4H-[1,2,4]triazolo[1,5-a]pyrimidin-7-one (28). The title compound was synthesized following the general procedure 1 with 3-amino-5-methyl-4*H*-1,2,4-triazole (150 mg, 1.5 mmol) and ethyl (4-fluorobenzoyl)acetate (0.301 mL, 1.7 mmol) to yield the title compound as an off-white solid (48 mg, yield 11 %). ^{1}H NMR (400 MHz, DMSO-d_6) δ 8.10–7.99 (m, 2H), 7.42–7.31 (m, 2H), 6.40 (s, 1H), 2.42 (s, 3H). t_R 1.24 min (generic method). ESI-MS for $C_{12}H_9FN_4O$: calculated 244.08, found *m/z* 243.2 M − and 245.0 M+.

4.3.2.7. 2-methyl-5-[4-(trifluoromethyl)phenyl]-4H-[1,2,4]triazolo[1,5-a]pyrimidin-7-one (29). The title compound was synthesized following the general procedure 1 with 3-amino-5-methyl-4*H*-1,2,4-triazole (138 mg, 1.41 mmol) and 3-oxo-3-(4-trifluoromethylphenyl)proprionic acid ethyl ester (0.321 mL, 1.56 mmol). The crude was purified by normal phase chromatography purification with a CombiFlash Rf Teledyne ISCO apparatus (12 g silica cartridge, solvent A: DCM, solvent B: DCM/MeOH & 1 N NH_3 4/1, gradient 0–82 % solvent B in 31 min) to yield the title compound as an off-white solid (14 mg, yield 3 %). ^{1}H NMR (400 MHz, DMSO-d_6) δ 8.20 (d, J = 8.2 Hz, 2H), 7.84 (d, J = 8.2 Hz, 2H), 6.44 (s, 1H), 2.40 (s, 3H). t_R 1.48 min (generic method). ESI-MS for $C_{13}H_9F_3N_4O$: calculated 294.07, found *m/z* 293.4 M − and 295.2 M+.

4.3.2.8. 2-methyl-5-(m-tolyl)-4H-[1,2,4]triazolo[1,5-a]pyrimidin-7-one (30). The title compound was synthesized following the general procedure 1 with 3-amino-5-methyl-4*H*-1,2,4-triazole (100 mg, 1 mmol) and 3-oxo-3-*m*-tolyl-propanoic acid ethyl ester (0.233 mL, 1.22 mmol). This was purified by normal phase column chromatography (12 g silica cartridge, solvent A: DCM, solvent B: DCM/MeOH 4/1 & NH_3, gradient 0–80 % solvent B in 21 min). To yield the title compound as a white solid (33 mg, 14 % yield). ^{1}H NMR (400 MHz, DMSO-d_6) δ 7.78 (d, J = 2.0 Hz, 1H), 7.72 (dd, J = 7.7, 2.0 Hz, 1H), 7.36 (t, J = 7.6 Hz, 1H), 7.28 (d, J = 7.5 Hz, 1H), 6.21 (s, 1H), 2.39 (s, 3H), 2.36 (s, 3H). ^{13}C NMR (125 MHz, DMSO-d_6) δ 158.27 (q), 156.80 (q), 156.78 (q), 156.27 (q), 154.28 (q), 137.77 (q), 136.27 (q), 130.48 (CH), 128.49 (CH), 127.63 (CH), 124.17 (CH), 95.24 (CH), 21.05 (CH_3), 13.95 (CH_3). t_R 1.31 min (generic method). ESI-MS for $C_{13}H_{12}N_4O$: calculated 240.1, found *m/z* 241.2 M+.

4.3.2.9. 2-methyl-5-(4-nitrophenyl)-4H-[1,2,4]triazolo[1,5-a]pyrimidin-7-one (31). The title compound was synthesized following the general procedure 1 with 3-amino-5-methyl-4*H*-1,2,4-triazole (100 mg, 1 mmol) and ethyl 4-nitrobenzoylacetate (237 mg, 1.2 mmol) to yield the title compound as an off-white solid (19 mg, yield 7 %). ^{1}H NMR (400 MHz, DMSO-d_6) δ 13.97 (s, 1H), 8.33 (d, J = 9.0 Hz, 2H), 8.26 (d, J = 8.9 Hz, 2H), 6.67 (s, 1H). t_R 1.24 min (generic method). ESI-MS for $C_{12}H_9N_5O_3$: calculated 271.07, found *m/z* 270.1 M − and 272.0 M+.

4.3.2.10. 5-(p-tolyl)-2-(trifluoromethyl)-4H-pyrazolo[1,5-a]pyrimidin-7-one (33). The title compound was synthesized following the general procedure 2 with 5-(trifluoromethyl)-1*H*-pyrazol-3-amine (61 mg, 0.40 mmol) and ethyl-3-oxo-3-(*p*-tolyl)propanoate (0.095 mL, 0.49 mmol) to yield the title compound as a white solid (29 mg, yield 23 %). ^{1}H NMR

(400 MHz, DMSO-d_6) δ 7.78 (d, J = 8.2 Hz, 2H), 7.41 (d, J = 8.0 Hz, 2H), 6.59 (s, 1H), 6.22 (s, 1H), 2.41 (s, 3H). ^{13}C NMR (101 MHz, DMSO-d_6) δ 156.28 (q), 151.38 (q), 144.34 (q), 143.97 (q), 143.44 (q), 142.07 (q), 130.15 (2x CH), 129.41 (q), 127.68 (2x CH), 94.65 (CH), 88.35 (CH), 21.39 (CH_3). t_R 1.86 min (generic method). ESI-MS for $C_{14}H_{10}F_3N_3O$: calculated 293.08, found *m/z* 292.1 M − and 294.0 M+.

4.3.2.11. 2-methyl-5-phenyl-4H-pyrazolo[1,5-a]pyrimidin-7-one (34). The title compound was synthesized following the general procedure 2 with 3-amino-5-methylpyrazole (84 mg, 0.87 mmol) and ethyl benzoylacetate (0.182 mL, 1.04 mmol) to yield the title compound as a white solid (104 mg, yield 54 %). ^{1}H NMR (400 MHz, DMSO-d_6) δ 7.89–7.81 (m, 2H), 7.56 (m, 3H), 6.03 (s, 1H), 5.99 (s, 1H), 2.31 (s, 3H). (101 MHz, DMSO-d_6) δ 156.83 (q), 152.50 (q), 150.47 (q), 143.78 (q), 133.59 (q), 131.20 (CH), 129.44 (2 x CH), 127.57 (2 x CH), 93.50 (CH), 90.03 (CH), 14.61 (CH3). t_R 1.30 min (generic method). ESI-MS for $C_{13}H_{11}N_3O$: calculated 225.09, found *m/z* 224.4 M − and 246.2 M+.

4.3.2.12. 2-methyl-5-(p-tolyl)-4H-pyrazolo[1,5-a]pyrimidin-7-one (35). The title compound was synthesized following the general procedure 2 with 5-(methyl)-1*H*-pyrazol-3-amine (543 mg, 5.6 mmol) and ethyl-3-oxo-3-(*p*-tolyl)propanoate (1.31 mL, 6.7 mmol) to yield the title compound as a pink solid (675 mg, yield 50 %). ^{1}H NMR (400 MHz, DMSO-d_6) δ 7.73 (d, J = 8.0 Hz, 2H), 7.38 (d, J = 8.0 Hz, 2H), 6.04 (s, 1H), 5.98 (s, 1H), 2.39 (s, 3H), 2.31 (s, 3H). ^{13}C NMR (101 MHz, DMSO-d_6) δ 156.62 (q), 152.53 (q), 149.66 (q), 142.94 (q), 141.46 (q), 130.07 (2x CH), 129.98 (q), 127.44 (2x CH), 93.52 (CH), 89.66 (CH), 21.37 (CH_3), 14.60 (CH_3). t_R 1.51 min (generic method). ESI-MS for $C_{14}H_{13}N_3O$: calculated 239.11, found *m/z* 238.4 M − and 240.2 M+.

4.3.2.13. 5-(p-tolyl)-4H-pyrazolo[1,5-a]pyrimidin-7-one (36). The title compound was synthesized following the general procedure 2 with 3-aminopyrazole (200 mg, 2.4 mmol) and ethyl-3-oxo-3-(*p*-tolyl)propanoate (0.517 mL, 2.65 mmol) to yield the title compound as a white solid (89 mg, yield 14 %). ^{1}H NMR (400 MHz, DMSO-d_6) δ 12.42 (s, 1H), 7.89 (d, J = 1.9 Hz, 1H), 7.81–7.70 (m, 2H), 7.47–7.34 (m, 2H), 6.22 (d, J = 1.9 Hz, 1H), 6.04 (s, 1H), 2.41 (s, 3H). ^{13}C NMR (101 MHz, DMSO-d_6) δ 156.96 (q), 150.12 (q), 143.48 (q), 142.37 (q), 141.61 (q), 130.09 (2x CH), 129.82 (q), 127.52 (2x CH), 93.54 (CH), 89.96 (CH), 21.36 (CH_3). t_R 1.43 min (generic method). ESI-MS for $C_{13}H_{11}N_3O$: calculated 225.09, found *m/z* 224.2 M − and 226.1 M+.

4.3.2.14. 2-ethyl-5-(p-tolyl)-4H-pyrazolo[1,5-a]pyrimidin-7-one (37). The title compound was synthesized following the general procedure 2 with 5-amino-3-ethyl-1*H*-pyrazole (200 mg, 1.8 mmol) and ethyl-3-oxo-3-(*p*-tolyl)propanoate (0.421 mL, 2.16 mmol). The crude was purified by normal phase chromatography purification with a CombiFlash Rf Teledyne ISCO apparatus (24 g silica cartridge, solvent A: DCM, solvent B: DCM/MeOH 4/1 & NH_3 gradient 0–48 % solvent B in 19 min) to yield the title compound as an off-white solid (142 mg, yield 31 %). ^{1}H NMR (400 MHz, DMSO-d_6) δ 12.27 (s, 1H), 7.78–7.69 (m, 2H), 7.41–7.34 (m, 2H), 6.04 (s, 1H), 5.97 (s, 1H), 2.68 (q, J = 7.6 Hz, 2H), 2.40 (s, 3H), 1.25 (t, J = 7.6 Hz, 3H). ^{13}C NMR (101 MHz, DMSO-d_6) δ 158.08 (q), 156.84 (q), 149.99 (q), 143.21 (q), 141.33 (q), 130.29 (q), 130.04 (2x CH), 127.44 (2x CH), 93.32 (CH), 88.41 (CH), 22.15 (CH_2), 21.37 (CH_3), 13.86 (CH_3). t_R 1.61 min (generic method). ESI-MS for $C_{15}H_{15}N_3O$: calculated 253.12, found *m/z* 252.3 M − and 254.2 M+.

4.3.2.15. 2-cyclopropyl-5-(p-tolyl)-4H-pyrazolo[1,5-a]pyrimidin-7-one (38). The title compound was synthesized following the general procedure 2 with 3-cyclopropyl-1*H*-pyrazol-5-amine (50 mg, 0.49 mmol) and ethyl (4-methylbenzoyl)acetate (0.095 mL, 0.41 mmol) to yield the title compound as a white solid (42 mg, 39 % yield). ^{1}H NMR (400 MHz, DMSO-d_6) δ 12.23 (s, 1H), 7.76–7.65 (m, 2H), 7.38 (d, J = 8.0 Hz, 2H), 5.96 (s, 1H), 5.93 (s, 1H), 2.39 (s, 3H), 2.01 (m, 1H), 0.97 (m, 2H), 0.82 (m, 2H). ^{13}C NMR (151 MHz, DMSO-d_6) δ 158.44 (C), 156.02 (C), 149.07 (C), 142.30 (C), 141.02 (C), 129.61 (2 X CH), 129.43 (C), 126.99 (2 X CH), 93.19 (CH), 86.20 (CH), 20.91(CH_3), 9.64 (CH), 8.63 (2 X CH_2). t_R 1.65 min (generic method). ESI-MS for $C_{16}H_{15}N_3O$: calculated 265.12, found *m/z* 264.3 M − and 266.2 M+.

4.3.2.16. 2-cyclobutyl-5-(p-tolyl)-4H-pyrazolo[1,5-a]pyrimidin-7-one (39). The title compound was synthesized following the general procedure 2 with 3-amino-5-cyclobutyl-1*H*-pyrazole (200 mg, 1.46 mmol) and ethyl-3-oxo-3-(*p*-tolyl)propanoate (0.343 mL, 1.75 mmol) to yield the title compound as an off-white solid (191 mg, yield 47 %). ^{1}H NMR (400 MHz, DMSO-d_6) δ 12.28 (s, 1H), 7.77–7.69 (m, 2H), 7.39 (d, J = 8.1 Hz, 2H), 6.08 (s, 1H), 5.98 (s, 1H), 3.67–3.53 (m, 1H), 2.40 (s, 3H), 2.37–2.17 (m, 4H), 2.02 (m, 1H), 1.95–1.81 (m, 1H). ^{13}C NMR (101 MHz, DMSO-d_6) δ 160.13 (q), 156.80 (q), 149.76 (q), 142.90 (q), 141.47 (q), 130.37 (q), 130.04 (2x CH) (d, J = 6.7 Hz), 127.47 (2x CH), 93.61 (CH), 87.39 (CH), 34.36 (CH_3), 28.81 (2 x CH_2), 21.37 (CH), 18.75 (CH_3). t_R 1.77 min (generic method). ESI-MS for $C_{17}H_{17}N_3O$: calculated 279.14, found *m/z* 278.3 M − and 280.2 M+.

4.3.2.17. 2-tert-butyl-5-(p-tolyl)-4H-pyrazolo[1,5-a]pyrimidin-7-one (40). The title compound was synthesized following the general procedure 2 with 3-(*tert*-butyl)-1*H*-pyrazol-5-amine (200 mg, 1.44 mmol) and ethyl-3-oxo-3-(*p*-tolyl)propanoate (0.338 mL, 1.73 mmol) to yield the title compound as an off-white solid (146 mg, yield 36 %). ^{1}H NMR (400 MHz, DMSO-d_6) δ 12.25 (s, 1H), 7.76–7.70 (m, 2H), 7.41–7.37 (m, 2H), 6.07 (s, 1H), 5.97 (s, 1H), 2.40 (s, 3H), 1.33 (s, 9H). ^{13}C NMR (101 MHz, DMSO-d_6) δ 165.12 (q), 156.88 (q), 149.75 (q), 142.67 (q), 141.47 (q), 130.09 (2x CH), 130.03 (q), 127.48 (2x CH), 93.58 (CH), 86.45 (CH), 32.89 (q), 30.56 (3x CH_3), 21.39 (CH_3). t_R 1.85 min (generic method). ESI-MS for $C_{17}H_{19}N_3O$: calculated 281.15, found *m/z* 280.3 M − and 282.2 M+.

4.3.2.18. 5-(p-tolyl)-2-(2-thienyl)-4H-pyrazolo[1,5-a]pyrimidin-7-one (41). The title compound was synthesized following the general procedure 2 with 5-amino-3-(2-thienyl)pyrazole (200 mg, 1.21 mmol) and ethyl-3-oxo-3-(*p*-tolyl)propanoate (0.283 mL, 1.21 mmol) to yield the title compound as a yellow solid (101 mg, yield 27 %). ^{1}H NMR (400 MHz, DMSO-d_6) δ 12.49 (s, 1H), 7.80–7.73 (m, 2H), 7.71 (dd, J = 3.6, 1.2 Hz, 1H), 7.63–7.61 (m, 1H), 7.43–7.38 (m, 2H), 7.17 (dd, J = 5.0, 3.6 Hz, 1H), 6.56 (s, 1H), 6.07 (s, 1H), 2.41 (s, 3H). ^{13}C NMR (101 MHz, DMSO-d_6) δ 156.55 (q), 150.18 (q), 149.41 (q), 143.52 (q), 141.67 (q), 136.02 (q), 130.10 (2x CH), 129.78 (q), 128.36 (CH), 127.56 (2x CH), 127.53 (CH), 127.22 (CH), 94.14 (CH), 86.82 (CH), 21.39 (CH_3). t_R 1.82 min (generic method). ESI-MS for $C_{17}H_{13}N_3OS$: calculated 307.08, found *m/z* 306.2 M − and 308.0 M+.

4.3.2.19. 4-methyl-5-(p-tolyl)-2-(trifluoromethyl)pyrazolo[1,5-a]pyrimidin-7-one (42). The title compound was synthesized following the general procedure 3 with 5-(*p*-tolyl)-25-(*p*-tolyl)-2-(trifluoromethyl)-4*H*-pyrazolo[1,5-a]pyrimidin-7-one (100 mg, 0.34 mmol), K_2CO_3 (188 mg, 1.36 mmol) in and iodomethane (212 μL, 3.4 mmol) to yield the title compound as a white solid (75 mg, yield 72 %). ^{1}H NMR (400 MHz, DMSO-d_6) δ 7.51–7.47 (m, 2H), 7.40 (d, J = 7.9 Hz, 2H), 7.07 (s, 1H), 5.86 (s, 1H), 3.52 (s, 3H), 2.41 (s, 3H). ^{13}C NMR (101 MHz, DMSO-d_6) δ 155.43 (q), 155.25 (q), 145.70 (q), 144.39 (q), 144.02 (q), 140.71 (q), 129.99 (q), 129.80 (2 x CH), 129.13 (2x CH), 99.11 (CH), 89.80 (CH), 38.51 (CH_3), 21.38 (CH_3). t_R 2.05 min (generic method). ESI-MS for $C_{15}H_{12}F_3N_3O$: calculated 307.09, found *m/z* 308.02 M+.

4.3.2.20. 4-ethyl-5-(p-tolyl)-2-(trifluoromethyl)pyrazolo[1,5-a]pyrimidin-7-one (43). The title compound was synthesized following the general procedure 3 with 5-(*p*-tolyl)-25-(*p*-tolyl)-2-(trifluoromethyl)-4*H*-pyrazolo[1,5-a]pyrimidin-7-one (100 mg, 0.34 mmol), K_2CO_3 (188 mg, 1.36 mmol) in and iodoethane (1.03 mL, 3.4 mmol). Purification was

carried out by normal phase chromatography purification with a CombiFlash Rf Teledyne ISCO apparatus (12 g silica cartridge, solvent A: DCM, solvent B: DCM/MeOH 4/1 gradient 0–27 % solvent B in 11 min) to yield the title compound as an off-white solid (75 mg, yield 69 %). ^{1}H NMR (400 MHz, DMSO-d_6) δ 7.49–7.45 (m, 2H), 7.39 (d, J = 7.9 Hz, 2H), 7.17 (s, 1H), 5.82 (s, 1H), 3.96 (q, J = 7.1 Hz, 2H), 2.41 (s, 3H), 1.13 (t, J = 7.1 Hz, 3H). ^{13}C NMR (101 MHz, DMSO-d_6) δ 155.11 (q), 144.56 (q), 144.20 (q), 140.51 (q), 130.01 (q), 129.84 (2x CH), 128.76 (2x CH), 123.00 (q), 120.32 (q), 99.79 (CH), 89.61 (CH), 45.78 (CH_2), 21.37 (CH_3), 13.63 (CH_3). t_R 2.19 min (generic method). ESI-MS for $C_{16}H_{14}F_3N_3O$: calculated 321.11, found m/z 322.2 M+.

4.3.2.21. 5-(m-tolyl)-2-(trifluoromethyl)-4H-pyrazolo[1,5-a]pyrimidin-7-one (44). The title compound was synthesized following the general procedure 2 with 5-(trifluoromethyl)-1*H*-pyrazol-3-amine (100 mg, 0.66 mmol), and ethyl 3-(3-methylphenyl)-3-oxopropanoate (0.151 mL, 0.79 mmol) to yield the title compound as an off-white solid (34 mg, 18 % yield). ^{1}H NMR (400 MHz, DMSO-d_6) δ 12.89 (s, 1H), 7.72–7.62 (m, 2H), 7.54–7.41 (m, 2H), 6.60 (s, 1H), 6.24 (s, 1H), 2.43 (s, 3H). ^{13}C NMR (101 MHz, DMSO-d_6) δ 156.28 (q), 151.59 (q), 144.20 (q), 143.47 (q), 139.08 (CH), 132.53 (q), 132.33 (q), 129.53 (CH), 128.28 (CH), 125.01 (CH), 120.38 (q), 95.08 (CH), 88.41 (CH), 21.40 (CH_3). t_R 1.81 min (generic method). ESI-MS for $C_{14}H_{10}F_3N_3O$: calculated 293.08, found m/z 292.2 M − and 294.1 M+.

4.3.2.22. 5-(4-bromophenyl)-2-(trifluoromethyl)-4H-pyrazolo[1,5-a]pyrimidin-7-one (45). The title compound was synthesized following the general procedure 2 with 3-amino-5-(trifluoromethyl)-pyrazole (100 mg, 0.66 mmol) and ethyl 3-(4-bromophenyl)-3-oxopropanoate (0.150 mL, 0.79 mmol) to yield the title compound as a yellow solid (58 mg, 25 % yield). ^{1}H NMR (400 MHz, DMSO-d_6) δ 12.98 (s, 1H), 7.82 (s, 4H), 6.62 (s, 1H), 6.28 (s, 1H). ^{13}C NMR (101 MHz, DMSO-d_6) δ 156.21 (q), 150.40 (q), 144.29 (q), 143.45 (q), 132.58 (q), 131.59 (q), 129.94 (2x CH), 125.59 (q), 123.03 (2x CH), 95.45 (CH), 88.52 (CH). t_R 1.83 min (generic method). ESI-MS for $C_{13}H_7BrF_3N_3O$: calculated 356.97, found m/z 356.1 M − and 358.0 M+.

4.3.2.23. 5-(3-bromophenyl)-2-(trifluoromethyl)-4H-pyrazolo[1,5-a]pyrimidin-7-one (46). The title compound was synthesized following the general procedure 2 with 3-amino-5-(triflouromethyl)-pyrazole (150 mg, 0.99 mmol) and ethyl (3-bromobenzoyl)acetate (0.223 mL, 1.18 mmol) to yield the title compound as a white solid (142 mg, yield 33 %). ^{1}H NMR (400 MHz, DMSO-d_6) δ 12.99 (s, 1H), 8.08 (t, J = 1.9 Hz, 1H), 7.91–7.85 (m, 1H), 7.83 (ddd, J = 8.1, 2.0, 0.9 Hz, 1H), 7.56 (t, J = 7.9 Hz, 1H), 6.63 (s, 1H), 6.31 (s, 1H). ^{13}C NMR (101 MHz, DMSO-d_6) δ 156.19 (q), 153.26 (q), 149.97 (q), 147.59 (q), 143.48 (q), 134.71 (q), 134.53 (CH), 131.69 (CH), 130.43 (CH), 127.16 (CH), 122.73 (q), 95.80 (CH), 88.54 (CH). t_R 1.81 min (generic method). ESI-MS for $C_{13}H_7BrF_3N_3O$: calculated 356.97, found m/z 356.3 M − and 358.0 M+.

4.3.2.24. 5-(4-fluorophenyl)-2-(trifluoromethyl)-4H-pyrazolo[1,5-a]pyrimidin-7-one (47). The title compound was synthesized following the general procedure 2 with 5-(trifluoromethyl)-1*H*-pyrazol-3-amine (100 mg, 0.66 mmol), and ethyl 3-(4-fluorophenyl)-3-oxopropanoate (0.167 mL, 0.79 mmol) to yield the title compound as an off-white solid (39 mg, 20 % yield). ^{1}H NMR (400 MHz, DMSO-d_6) δ 12.94 (s, 1H), 7.99–7.90 (m, 2H), 7.51–7.42 (m, 2H), 6.61 (s, 1H), 6.25 (s, 1H). ^{13}C NMR (101 MHz, DMSO-d_6) δ 165.62 (q), 163.14 (q), 156.22 (q), 150.52 (q), 144.25 (q), 143.42 (q), 130.52 (2 x CH), 128.90 (q), 116.66 (2x CH), 95.28 (CH), 88.45 (CH). t_R 1.67 min (generic method). ESI-MS for $C_{13}H_7F_4N_3O$: calculated 297.05, found m/z 296.2 M − and 298.1 M+.

4.3.2.25. 2-(trifluoromethyl)-5-[3-(trifluoromethyl)phenyl]-4H-pyrazolo [1,5-a]pyrimidin-7-one (48). The title compound was synthesized following the general procedure 2 with 5-(trifluoromethyl)-1*H*-pyrazol-3-amine (100 mg, 0.66 mmol) and 3-oxo-3-(3-trifluoromethylphenyl) propanoic acid ethyl ester (0.162 mL, 0.79 mmol) to yield the title compound as an off-white solid (47 mg, 21 % yield). ^{1}H NMR (400 MHz, DMSO-d_6) δ 13.08 (s, 1H), 8.22 (s, 1H), 8.18 (d, J = 8.1 Hz, 1H), 8.00 (d, J = 7.9 Hz, 1H), 7.85 (t, J = 7.8 Hz, 1H), 6.66 (s, 1H), 6.39 (s, 1H). t_R 1.99 min (generic method). ESI-MS for $C_{14}H_7F_6N_3O$: calculated 347.05, found m/z 346.0 M − and 348.0 M+.

4.3.2.26. 5-(3-fluorophenyl)-2-(trifluoromethyl)-4H-pyrazolo[1,5-a]pyrimidin-7-one (49). The title compound was synthesized following the general procedure 2 with 5-(trifluoromethyl)-1*H*-pyrazol-3-amine (100 mg, 0.66 mmol) and ethyl 3-(3-fluorophenyl)-3-oxopropanoate (0.143 mL, 0.79 mmol) to yield the title compound as an off-white solid (41 mg, 21 % yield). ^{1}H NMR (400 MHz, DMSO-d_6) δ 12.97 (s, 1H), 7.79–7.71 (m, 2H), 7.66 (td, J = 8.0, 5.8 Hz, 1H), 7.52–7.43 (m, 1H), 6.63 (s, 1H), 6.33 (s, 1H). ^{13}C NMR (101 MHz, DMSO-d_6) δ 156.20 (q), 150.01 (q), 144.37 (q), 143.47 (q), 133.52 (CH), 132.23 (CH), 130.82 (CH), 130.24 (q), 128.36 (q), 124.68 (CH), 122.99 (q), 96.15 (CH), 88.56 (CH).t_R 1.84 min (generic method). ESI-MS for $C_{13}H_7F_4N_3O$: calculated 297.06, found m/z 296.0 M − and 298.0 M+.

4.3.2.27. 5-(4-nitrophenyl)-2-(trifluoromethyl)-4H-pyrazolo[1,5-a]pyrimidin-7-one (50). The title compound was synthesized following the general procedure 2 with 5-(trifluoromethyl)-1*H*-pyrazol-3-amine (100 mg, 0.66 mmol) and ethyl-3-(4-nitrophenyl)-3-oxopropanoate (188 mg, 0.79 mmol) to yield the title compound as an off white solid (47.1 mg,21 % yield). ^{1}H NMR (400 MHz, DMSO-d_6) δ 8.50–8.37 (m, 2H), 8.19–8.09 (m, 2H), 6.67 (s, 1H), 6.38 (s, 1H). ^{13}C NMR (101 MHz, DMSO-d_6) δ 156.10 (q), 149.45 (q), 149.39 (q), 144.28 (q), 143.49 (q), 138.42 (q), 129.55 (2x CH), 124.51 (2x CH), 120.31 (q), 96.78 (CH), 88.72 (CH). t_R 1.61 min (generic method). ESI-MS for $C_{13}H_7F_3N_4O_3$: calculated 324.05, found m/z 323.3 M − and 325.1 M+.

4.3.2.28. 5-(4-aminophenyl)-2-(trifluoromethyl)-4H-pyrazolo[1,5-a]pyrimidin-7-one (51). Under argon atmosphere, to 5-(4-nitrophenyl)-2-(trifluoromethyl)-4H-pyrazolo[1,5-*a*]pyrimidin-7-one (50 mg, 0.15 mmol) and palladium hydroxide on carbon (10 mg) in methanol (3 mL) was added ammonium formate (38 mg, 0.6 mmol) and the reaction crude was stirred at reflux for 30 min. The reaction crude was then filtered through Celite and washed twice with methanol (2 × 5 mL). The solvent was evaporated *in vacuo* to yield a yellow solid (44 mg, 99 % yield). ^{1}H NMR (400 MHz, DMSO-d_6) δ 12.47 (s, 1H), 7.64–7.55 (m, 2H), 6.73–6.64 (m, 2H), 6.52 (s, 1H), 6.08 (s, 1H), 5.92 (s, 2H). ^{13}C NMR (101 MHz, DMSO-d_6) δ 156.38 (q), 152.71 (q), 151.89 (q), 144.34 (q), 143.96 (q), 143.53 (q), 128.94 (CH x 2), 117.92 (q), 113.95 (CH x 2), 91.71 (CH), 88.02 (CH). t_R 1.50 min (generic method). ESI-MS for $C_{13}H_9F_3N_4O$: calculated 294.07, found m/z 293.0 M − and 295.0 M+.

4.3.2.29. 5-methyl-2-(trifluoromethyl)-4H-pyrazolo[1,5-a]pyrimidin-7-one (52). The title compound was synthesized following the general procedure 2 with 5-(trifluoromethyl)-1*H*-pyrazol-3-amine (100 mg, 0.66 mmol) and ethyl acetoacetate (0.1 mL, 0.79 mmol) to yield the title compound as an off-white solid (102 mg, yield 72 %).^{1}H NMR (400 MHz, DMSO-d_6) δ 12.71 (s, 1H), 6.55 (s, 1H), 5.76 (s, 1H), 2.34 (s, 3H). ^{13}C NMR (101 MHz, DMSO-d_6) δ 156.02 (q), 152.33 (q), 143.09 (q), 123.08 (q), 120.40 (q), 96.45 (CH), 87.29 (CH), 19.23 (CH_3). t_R 1.35 min (generic method). ESI-MS for $C_8H_6F_3N_3O$: calculated 217.05, found m/z 161.1 M − and 218.0 M+.

4.3.2.30. 5-cyclopropyl-2-(trifluoromethyl)-4H-pyrazolo[1,5-a]pyrimidin-7-one (53). The title compound was synthesized following the general procedure 2 with 5-(trifluoromethyl)-1*H*-pyrazol-3-amine (100 mg, 0.66 mmol) and ethyl-3-cyclopropyl-3-oxopropionate (0.116 mL, 0.79 mmol) to yield the title compound as an off-white solid (59 mg, yield 37 %). ^{1}H NMR (400 MHz, DMSO-d_6) δ 12.57 (s, 1H), 6.50 (s, 1H), 5.59 (s,

1H), 2.00–1.88 (m, 1H), 1.18–0.97 (m, 4H). ^{13}C NMR (101 MHz, DMSO-d_6) δ 158.09 (q), 156.08 (q), 143.99 (q), 143.62 (q), 142.99 (q), 91.70 (CH), 87.36 (CH), 13.64 (CH), 9.97 (2x CH_2). t_R 1.54 min (generic method). ESI-MS for $C_{10}H_8F_3N_3O$: calculated 243.06, found *m/z* 242.1 M − and 244.0 M+.

4.3.2.31. 5-(difluoromethyl)-2-(trifluoromethyl)-4H-pyrazolo[1,5-a]pyrimidin-7-one (54). The title compound was synthesized following the general procedure 2 with 5-(trifluoromethyl)-1*H*-pyrazol-3-amine (100 mg, 0.66 mmol) and ethyl 4,4-difluoroacetoacetate (0.104 mL, 0.79 mmol). The reaction mixture was partitioned between water (10 mL), sodium bicarbonate (10 mL) and EtOAc (20 mL), then the aq. phase extracted with EtOAc (2 × 10 mL). The combined organics were dried ($MgS0_4$) and evaporated *in vacuo* to yield the reaction crude. Purification was carried out using normal phase chromatography purification with a CombiFlash Rf Teledyne ISCO apparatus (12 g silica cartridge, solvent A: DCM, solvent B: DCM/Methanol (4:1) &1 N NH_3, gradient 0–98 % solvent B in 18 min) to yield the title compound as a white solid (65 mg, yield 39 %). ^{1}H NMR (400 MHz, DMSO-d_6) δ 7.08 (t, J = 53.3 Hz, 1H), 6.68 (s, 1H), 6.22 (s, 1H). ^{13}C NMR (101 MHz, DMSO-d_6) δ 155.88 (q), 143.30 (q), 120.21 (q), 113.51 (q), 111.12 (CH), 108.72 (q), 96.34 (CH), 89.03 (CH). t_R 1.18 min (generic method). ESI-MS for $C_8H_4F_5N_3O$: calculated 253.03, found *m/z* 252.0 M − and 353.9 M+.

4.3.2.32. 5-(2-pyridyl)-2-(trifluoromethyl)-4H-pyrazolo[1,5-a]pyrimidin-7-one (55). The title compound was synthesized following the general procedure 2 with 5-(trifluoromethyl)-1*H*-pyrazol-3-amine (50 mg, 0.33 mmol) and ethyl picolinoylacetate (0.065 mL, 0.4 mmol) to yield the title compound as a white solid (42 mg, yield 45 %). ^{1}H NMR (400 MHz, DMSO-d_6) δ 13.06 (s, 1H), 8.84 (dt, J = 4.7, 1.4 Hz, 1H), 8.40–8.31 (m, 1H), 8.08 (td, J = 7.8, 1.7 Hz, 1H), 7.66 (ddd, J = 7.6, 4.8, 1.0 Hz, 1H), 6.81 (s, 1H), 6.66 (s, 1H). ^{13}C NMR (151 MHz, DMSO-d_6) δ 156.25 (C), 149.41, 147.65, 147.33, 143.84 (J = 35.6 Hz, -*C*-CF_3), 143.07, 138.23, 126.34, 122.39, 121.31 (J = 281.7 Hz, -*C*F_3), 94.12 (CH), 88.75 (J = 2.7 Hz, -*C*-C-CF_3). t_R 1.47 min (generic method). ESI-MS for $C_{12}H_7F_3N_4O$: calculated 280.06, found *m/z* 279.0 M and 281.0 M+.

4.3.2.33. 5-(5-bromo-3-pyridyl)-2-(trifluoromethyl)-4H-pyrazolo[1,5-a]pyrimidin-7-one (56). The title compound was synthesized following the general procedure 2 with 5-(trifluoromethyl)-1*H*-pyrazol-3-amine (150 mg, 1 mmol), and methyl 5-bromonicotinoylacetate (281 mg, 1.1 mmol) The resulting crude was purified by normal phase chromatography purification with a CombiFlash Rf Teledyne ISCO apparatus (12 g silica cartridge, solvent A: DCM, solvent B: DCM/MeOH 4/1, gradient 0–30 % solvent B in 18 min). To yield the title compound as an off white solid (111 mg, 31 % yield). ^{1}H NMR (400 MHz, DMSO-d_6) δ 13.15 (s, 1H), 9.04 (d, J = 2.0 Hz, 1H), 8.93 (d, J = 2.1 Hz, 1H), 8.55 (t, J = 2.1 Hz, 1H), 6.68 (s, 1H), 6.44 (s, 1H). ^{13}C NMR (101 MHz, DMSO-d_6) δ 156.03 (q), 152.96 (q), 147.54 (q), 147.30 (q), 144.44 (q), 143.42 (CH), 138.06 (CH), 130.21 (CH), 122.99 (q), 120.72 (CH), 96.63 (CH), 88.62 (CH). t_R 1.61 min (generic method). ESI-MS for $C_{12}H_6BrF_3N_4O$: calculated 357.96, found *m/z* 357.1 M − and 358.9 M+.

4.3.3. Kinetic solubility studies

The aqueous kinetic solubility in High-Throughput was determined from a 10 mM DMSO stock solution of test compound in Phosphate Buffered Saline (PBS) at pH 7.4. The study was performed in a Multi-Screen Solubility Filter Plate by incubation of an aliquot of 10 mM DMSO stock solution in PBS (pH 7.4) at a target concentration of 250 μM (2.5 % DMSO). The incubation was carried out under shaking at 25 °C for 24 h followed by filtration under vacuum. The filtrate was further diluted (4:1) with CH_3CN and dissolved test compound was quantified by UV at 215 nm on a Waters ACQUITY UPLC-MS system from Waters Inc. (Milford, MA, USA). The system consisted of a Single Quadrupole Detector (SQD) mass spectrometer equipped with an Electrospray Ionization interface and a Photodiode Array Detector. Electrospray ionization in positive mode was used in the mass scan range 100–500 Da. The PDA range was 210–400 nm. The analyses were run on an ACQUITY UPLC BEH C18 column (50 × 2.1 mmID, particle size 1.7 μm) with a VanGuard BEH C18 pre-column (5 × 2.1mmID, particle size 1.7 μm), using 10 mM NH_4OAc in H_2O at pH 5 adjusted with AcOH (A) and 10 mM NH_4OAc in CH_3CN–H_2O (95:5) at pH 5 (B) as mobile phase. The aqueous kinetic solubility (in μM) was calculated by dividing the peak areas of dissolved test compound and test compound in reference (250 μM of test compound in CH_3CN), multiplied by the target concentration and dilution factor.

4.4. Biological experiments

4.4.1. ELISA assay

Competitive ELISA screening assay using biotinylated BRC4 peptide to disrupt the BRC4-RAD51 interaction was performed by modifying the method described by Rajendra et al. [27] BRC4-biotinylated peptide (N-term biotin-KEPTLLGFH-TASGKKVKIAKESLDKVKNLFDEKEQ from Life Technologies) was used to coat 384-well plates (Nunc). After washing with PBS containing 0.05 % Tween-20 (PBST) and blocking with the solution BSA 1 %/PBST, overnight hybridization with human RAD51 protein (NP_002866 Creative Biomart, NY) was performed. Test compounds were added in dose response from 0.01 to 100 μM in triplicate with constant DMSO 1 %. Antibody raised against RAD51 (Millipore) and HRP-secondary antibody staining to develop the 3,3′,5,5′-tetramethylbenzidine signal (Sigma) quenched with 1 M HCl was used as the assay readout. Colorimetric measure was read on a Victor5 (PerkinElmer) plate reader. BRC4 and RAD51 were included in the assay as positive control. Results were analyzed by using GraphPadsoftware. The procedure was previously reported in Bagnolini G. et al. [16].

4.4.2. Cell cultures

Three different pancreatic ductal adenocarcinoma cell lines were used: BxPC-3 cells were grown in RPMI 1640 (R0883) supplemented with 10 % FBS, 100 U/mL penicillin/streptomycin, 2 mM glutamine; AsPC-1 and HPAC cells were grown in RPMI 1640 supplemented with 5 % FBS, 100 U/mL penicillin/streptomycin, 2 mM glutamine. HEK293 cell line was grown in DMEM High Glucose (D6546) supplemented with 10 % FBS, 100 U/mL penicillin/streptomycin, and 2 mM glutamine. All media and supplements were from Sigma-Aldrich. The human primary pancreatic epithelial cell line (Cell Biologics, H6037) was grown in its specific medium (Cell biologics, H6621) supplemented with epithelial cell growth supplement (Cell biologics, H6621-Kit). All the cell line cultures were routinely tested for Mycoplasma contamination.

4.4.3. Organoid cultures

The PT291 organoid was derived from xenografts of invasive pancreatic adenocarcinoma/cholangiocarcinoma of a female patient as previously described [57,58]. The PDM41 organoid (pancreatic ductal adenocarcinoma) was commercially available and provided by ATCC (HCM-CSHL-0094-C25). The Complete Human Feeding Media (CHFM) components were as follows: DMEM/F12 GlutaMAX™ Supplement (Thermofisher, 10565018), Antibiotic Antimycotic 100 X (Sigma-Aldrich, A5955), L-WRN (Wnt3a-R-spondin3 Noggin) conditioned media (50 % v/v), 500 nM A83-01 (Sigma-Aldrich, SML0788), 50 ng/mL EGF (ThermoFisher, PHG0311), 100 ng/mL hFGF10 (Biolegend, 559308), 0.01 μM Gastrine (Tocris, 3006), 1.25 mM N-acetylcysteine (R&D, 5619), 10 mM Nicotinammide (Sigma-Aldrich, N0636), B-27 Supplement 1X (Life Technologies, 17504-044)) 10.5 μM ROCKi (Sigma-Aldrich, Y-27632). The organoid establishment was performed as follows: cells were resuspended in Cultrex BME (R&D System Biotechne, 3432-005-01); 20 μL of organoid in BME solution was pipetted on to a 24-multiwell poly-HEMA coated plate. The plate was placed at 37 °C for 15 min to allow the BME to polymerize, and then CHFM with 10.5 μM ROCKi was added to each well. Two days after establishing the organoid

sample, cells were fed using CHFM without ROCKi, then subsequently fed every two days.

4.4.4. Homologous recombination Quick Assay (HR-QA)

Homologous recombination (HR) was assessed using a commercially available kit (Norgen, 35600). This assay is based on cell transfection with two plasmids able to recombine upon cell entry. The efficiency of HR was assessed by Real-Time PCR, using primer mixtures included in the assay kit. Different primer mixtures allow differentiation between the original plasmid backbones and their recombination product. Briefly, BxPC3 cells (2×10^5 per well) were seeded in a 24-well plate and allowed to adhere overnight. Co-transfection with the two plasmids (1 μg each) was performed in Lipofectamine 2000 (Invitrogen, 11668019, Waltham, MA, USA), according to the manufacturer's instructions. During the 5 h of transfection, cells were exposed to different doses of compounds, dissolved in DMSO. After washing with PBS, cells were harvested, and DNA was isolated using QIAamp DNA Mini kit (Qiagen, 51304). Sample concentration was measured using an ONDA Nano Genius photometer. The efficiency of HR was assessed by Real-Time PCR, using 25 ng of template and primer mixtures included in the assay kit, following the protocol indicated by the manufacturer. Data analysis was based on the $2^{-\Delta\Delta Ct}$ method: (Recombination Product/Backbone Plasmids) treated versus (Recombination Product/Backbone Plasmids) control.

4.4.5. mClover-based homologous recombination assay (mCL-HR)

50 μM **46** was added to HEK293 cells grown on coverslips in a 24 well plate 1 h before transfection. Cells were transfected with 500 ng sgRNA plasmid targeting Lamin A (pUC CBA-SpCas9.EF1a-BFP. sgLMNA, Addgene Plasmid, 98971) and 500 ng donor plasmid (pCAGGS Donor mClover-LMNA, Addgene Plasmid, 98970) using Lipofectamin2000 (Invitrogen, 11668019). The next day, cell culture media was replaced by fresh media containing 50 μM **46**. 3 days after transfection, cells were fixed in PBS containing 4 % formalin for 15 min and washed twice with PBS before mounting. Images acquired using a Nikon fluorescent microscope equipped with filters for FITC, TRITC and DAPI were analyzed by using the Cell Counter Plug-in of the ImageJ software.

4.4.6. Cells immunofluorescence assay

Immunofluorescence was used for studying RAD51 nuclear translocation. To visualize RAD51 in cell nuclei, BxPC-3 cells were seeded on glass coverslips placed in a 6-well culture plate (2×10^5 cells/well) and allowed to adhere overnight. Cultures were then preincubated with 30 μM **46** for 1 h and subsequently exposed to 50 μM cisplatin for an additional 1.5 h. Medium was removed, and cells were maintained in the presence of 30 μM **46** for 5 h. After this time, cultures growing on coverslips were fixed in PBS containing 4 % formalin for 13 min, permeabilized in 70 % ethanol, air-dried, and washed twice with PBS. Samples were incubated in 5 % bovine serum albumin (BSA) in PBS for 30 min and subsequently exposed to anti-RAD51 rabbit monoclonal antibody (1:1000 in 5 % BSA/PBS, BioAcademia, 70-001) overnight at 4 °C. After washing, coverslips were incubated with a secondary anti-rabbit rhodamine-labeled (Novus Biologicals, 1:1000 in 5 % BSA/PBS), for 30 min, washed, air-dried, and mounted with a solution 2 μg/mL DAPI in DABCO. Images were acquired using a Nikon fluorescent microscope equipped with filters for FITC, TRITC and DAPI. The percentage of cells bearing RAD51 nuclear foci was estimated by two independent observers analyzing approximately 200 cells for each treatment sample.

4.4.7. Cell viability assay

Cell viability was assessed with the PrestoBlue cell viability kit (Thermofisher, A13261). 1–10 $\times$ 10^3 cells, depending on cell type and incubation time, in 200 μL of culture medium, were seeded in a 96-multiwell plate, and allowed to adhere overnight. The day after, cells were treated with different doses of compounds, alone or in combination. After 6 days of treatment, 20 μL of the PrestoBlue cell Viability Reagent was added to each well, and incubated for 4 h at 37 °C. The fluorescence intensity was measured with the i-control™ Microplate Reader Software by Tecan.

4.4.8. Cell death inhibitors

BxPC-3 and HPAC cells were seeded in a 96-multiwell plate and allowed to adhere overnight. The day after, cells were treated with 2 μM talazoparib and 30 μM **46**, alone and in combination. 72 h later, 20 μM Z-VAD-FMK or 20 μM Nec-1 (Sigma–Aldrich, 627610; 480065) was added, and then re-added to cultures every 24 h until the sixth day of treatment. The cell viability was assessed by using the PrestoBlue cell viability kit (Thermofisher, A13261), as described previously.

4.4.9. Organoid viability assay

Organoid viability was assessed using the CellTiter-Glo® 3D Cell Viability Assay (Promega, G9681). 5 $\times$ 10^3 cells in 10 μL of Cultrex Basement Membrane were seeded into each well of a 96-multiwell polyHEMA-coated black-sided, clear bottom plate. The plate was incubated at 37 °C for 20 min to allow the BME to solidify; then, 100 μL of CHFM, supplemented with ROCKi, was added to each well. After 3 days, organoids were treated with 2X concentration of talazoparib and **46** in 100 μL of CHFM, and maintained for 6 days, alone or in combination. At the end of the treatment, 25 μL of the viability reagent was added to each well. After 5 min shaking and 25 min room temperature incubation, the luminescence intensity was measured with the i-control™ Microplate Reader Software by Tecan.

4.4.10. Immunofluorescence organoid assay

PT291 was seeded on glass coverslips placed in an 8-chamber plate (1×10^4 cells/well) and allowed to adhere and grow for 3 days. PT291 was treated with 50 μM **46** for 24 h. Medium was removed, and organoids were washed with PBS containing 0.1 % Tween and 2 % BSA (wash buffer) for 5 min. Then, they were fixed in 4 % Formalin in PBS for 20 min, permeabilized in 0.5 % Triton-X for 45 min, and washed twice with the wash buffer. Samples were blocked for 1.5 h with 10 % FBS in PBS and subsequently exposed to the anti- γ-H2AX mouse monoclonal antibody (BioAcademia, 1:250 in wash buffer) overnight at 4 °C. After washing, coverslips were incubated with an anti-mouse FITC-conjugated secondary antibody (Novus Biologicals, 1:200 in wash buffer) for 1 h at room temperature, washed, and counterstained with DAPI for 5 min. Images were acquired using Nikon fluorescent microscope equipped with filters for FITC, TRITC and DAPI. Images were analyzed by using the Cell Counter Plug-in of the ImageJ software.

CRediT authorship contribution statement

Samuel H. Myers: Writing – review & editing, Writing – original draft, Visualization, Methodology, Investigation, Data curation, Conceptualization. **Laura Poppi:** Writing – review & editing, Writing – original draft, Visualization, Methodology, Investigation, Data curation, Conceptualization. **Francesco Rinaldi:** Writing – review & editing, Writing – original draft, Visualization, Methodology, Investigation, Data curation, Conceptualization. **Marina Veronesi:** Methodology, Investigation, Conceptualization. Writing – review & editing, Writing – original draft, Data curation.**Andrea Ciamarone:** Writing – review & editing, Writing – original draft, Methodology, Investigation. **Viola Previtali:** Writing – review & editing, Investigation, Conceptualization. **Greta Bagnolini:** Writing – review & editing, Writing – original draft, Conceptualization. **Fabrizio Schipani:** Writing – review & editing, Methodology, Conceptualization. **Jose Antonio Ortega Martínez:** Writing – review & editing, Supervision, Methodology, Conceptualization. **Stefania Girotto:** Writing – review & editing, Writing – original draft, Supervision, Conceptualization. Methodology.**Giuseppina Di Stefano:** Writing – review & editing, Writing – original draft, Supervision, Conceptualization. **Fulvia Farabegoli:** Writing – review & editing,

Writing – original draft, Supervision, Conceptualization. **Naomi Walsh:** Writing – review & editing, Supervision, Methodology. **Francesca De Franco:** Writing – review & editing, Methodology, Investigation, Conceptualization. **Marinella Roberti:** Writing – review & editing, Writing – original draft, Supervision, Conceptualization. **Andrea Cavalli:** Writing – review & editing, Supervision, Project administration, Funding acquisition, Conceptualization.

Declaration of competing interest

The authors declare the following financial interests/personal relationships which may be considered as potential competing interests:

Andrea Cavalli reports financial support was provided by Associazione Italiana Ricerca sul Cancro AIRC (Progetto IG2018, id 21386). Francesco Rinaldi reports financial support by the same funding agency (AIRC Fellowship 2020, Id.25239). If there are other authors, they declare that they have no known competing financial interests or personal relationships that could have appeared to influence the work reported in this paper.

Data availability

No data was used for the research described in the article.

Acknowledgements

This work was supported by the Italian Association for Cancer Research (AIRC, IG 2018, id 21386), the Italian Institute of Technology (IIT), and the University of Bologna. Francesco Rinaldi is the recipient of an AIRC Fellowship 2020 “Ignazia-La-Russa” Id.25239.

We thank Dr. Claudio Dalvit for the fruitful scientific discussions.

Appendix A. Supplementary data

Supplementary data to this article can be found online at https://doi.org/10.1016/j.ejmech.2023.116114.

References

[1] J. Moon, I. Kitty, K. Renata, S. Qin, F. Zhao, W. Kim, DNA damage and its role in cancer therapeutics, Int. J. Mol. Sci. 24 (5) (2023), https://doi.org/10.3390/ijms24054741.

[2] R. Huang, P.K. Zhou, DNA damage repair: historical perspectives, mechanistic pathways and clinical translation for targeted cancer therapy, Signal Transduct. Targeted Ther. 6 (1) (2021) 254, https://doi.org/10.1038/s41392-021-00648-7.

[3] K.N. Maxwell, S.M. Domchek, K.L. Nathanson, M.E. Robson, Population frequency of germline BRCA1/2 mutations, J. Clin. Oncol. 34 (34) (2016) 4183–4185, https://doi.org/10.1200/jco.2016.67.0554.

[4] G. Bagnolini, D. Milano, M. Manerba, F. Schipani, J.A. Ortega, D. Gioia, F. Falchi, A. Balboni, F. Farabegoli, F. De Franco, et al., Synthetic lethality in pancreatic cancer: discovery of a new RAD51-BRCA2 small molecule disruptor that inhibits homologous recombination and synergizes with olaparib, J. Med. Chem. (2020), https://doi.org/10.1021/acs.jmedchem.9b01526.

[5] S.H. Myers, J.A. Ortega, A. Cavalli, Synthetic lethality through the lens of medicinal chemistry, J. Med. Chem. 63 (23) (2020) 14151–14183, https://doi.org/10.1021/acs.jmedchem.0c00766.

[6] M.R. Mirza, B.J. Monk, J. Herrstedt, A.M. Oza, S. Mahner, A. Redondo, M. Fabbro, J.A. Ledermann, D. Lorusso, I. Vergote, et al., Niraparib maintenance therapy in platinum-sensitive, recurrent ovarian cancer, N. Engl. J. Med. 375 (22) (2016) 2154–2164, https://doi.org/10.1056/NEJMoa1611310.

[7] J.K. Litton, H.S. Rugo, J. Ettl, S.A. Hurvitz, A. Goncalves, K.H. Lee, L. Fehrenbacher, R. Yerushalmi, L.A. Mina, M. Martin, et al., Talazoparib in patients with advanced breast cancer and a germline BRCA mutation, N. Engl. J. Med. 379 (8) (2018) 753–763, https://doi.org/10.1056/NEJMoa1802905.

[8] T. Golan, P. Hammel, M. Reni, E. Van Cutsem, T. Macarulla, M.J. Hall, J.O. Park, D. Hochhauser, D. Arnold, D.Y. Oh, et al., Maintenance olaparib for germline BRCA-mutated metastatic pancreatic cancer, N. Engl. J. Med. 381 (4) (2019) 317–327, https://doi.org/10.1056/NEJMoa1903387.

[9] A. Tripathi, P. Balakrishna, N. Agarwal, PARP inhibitors in castration-resistant prostate cancer, Cancer Treatment and Research Communications 24 (2020) 100199, https://doi.org/10.1016/j.ctarc.2020.100199.

[10] N.S. Nagathihalli, G. Nagaraju, RAD51 as a potential biomarker and therapeutic target for pancreatic cancer, Biochim. Biophys. Acta 1816 (2) (2011) 209–218, https://doi.org/10.1016/j.bbcan.2011.07.004.

[11] X. Zhang, N. Ma, W. Yao, S. Li, Z. Ren, RAD51 is a potential marker for prognosis and regulates cell proliferation in pancreatic cancer, Cancer Cell Int. 19 (2019) 356, https://doi.org/10.1186/s12935-019-1077-6.

[12] F. Falchi, E. Giacomini, T. Masini, N. Boutard, L. Di Ianni, M. Manerba, F. Farabegoli, L. Rossini, J. Robertson, S. Minucci, et al., Synthetic lethality triggered by combining olaparib with BRCA2-rad51 disruptors, ACS Chem. Biol. 12 (10) (2017) 2491–2497, https://doi.org/10.1021/acschembio.7b00707.

[13] M. Roberti, F. Schipani, G. Bagnolini, D. Milano, E. Giacomini, F. Falchi, A. Balboni, M. Manerba, F. Farabegoli, F. De Franco, et al., Rad51/BRCA2 disruptors inhibit homologous recombination and synergize with olaparib in pancreatic cancer cells, Eur. J. Med. Chem. 165 (2019) 80–92, https://doi.org/10.1016/j.ejmech.2019.01.008.

[14] L. Pellegrini, D.S. Yu, T. Lo, S. Anand, M. Lee, T.L. Blundell, A.R. Venkitaraman, Insights into DNA recombination from the structure of a RAD51–BRCA2 complex, Nature 420 (6913) (2002) 287–293, https://doi.org/10.1038/nature01230.

[15] D.E. Scott, N.J. Francis-Newton, M.E. Marsh, A.G. Coyne, G. Fischer, T. Moschetti, A.R. Bayly, T.D. Sharpe, K.T. Haas, L. Barber, et al., A small-molecule inhibitor of the BRCA2-RAD51 interaction modulates RAD51 assembly and potentiates DNA damage-induced cell death, Cell Chem. Biol. 28 (6) (2021) 835–847, https://doi.org/10.1016/j.chembiol.2021.02.006, e835.

[16] G. Bagnolini, B. Balboni, F. Schipani, D. Gioia, M. Veronesi, F. De Franco, C. Kaya, R.P. Jumde, J.A. Ortega, S. Girotto, et al., Identification of RAD51–BRCA2 inhibitors using N-Acylhydrazone-Based dynamic combinatorial chemistry, ACS Med. Chem. Lett. 13 (8) (2022) 1262–1269, https://doi.org/10.1021/acsmedchemlett.2c00063.

[17] P. Śledź, C. Abell, A. Ciulli, Ligand-observed NMR in fragment-based approaches, in: NMR of Biomolecules, 2012, pp. 264–280.

[18] L.G. Mureddu, G.W. Vuister, Fragment-based drug discovery by NMR. Where are the successes and where can it Be improved? Front. Mol. Biosci. 9 (2022) https://doi.org/10.3389/fmolb.2022.834453. Original Research.

[19] A. Vulpetti, U. Hommel, G. Landrum, R. Lewis, C. Dalvit, Design and NMR-based screening of LEF, a library of chemical fragments with different local environment of fluorine, J. Am. Chem. Soc. 131 (36) (2009) 12949–12959. https://doi.org/10.1021/ja905207t.

[20] D.A. Erlanson, S.W. Fesik, R.E. Hubbard, W. Jahnke, H. Jhoti, Twenty years on: the impact of fragments on drug discovery, Nat. Rev. Drug Discov. 15 (9) (2016) 605–619, https://doi.org/10.1038/nrd.2016.109.

[21] D.E. Scott, M.T. Ehebauer, T. Pukala, M. Marsh, T.L. Blundell, A.R. Venkitaraman, C. Abell, M. Hyvonen, Using a fragment-based approach to target protein-protein interactions, Chembiochem 14 (3) (2013) 332–342, https://doi.org/10.1002/cbic.201200521.

[22] C. Dalvit, M. Flocco, M. Veronesi, B.J. Stockman, Fluorine-NMR competition binding experiments for high-throughput screening of large compound mixtures, Comb. Chem. High Throughput Screening 5 (8) (2002) 605–611, https://doi.org/10.2174/1386207023329923.

[23] C. Dalvit, P.E. Fagerness, D.T. Hadden, R.W. Sarver, B.J. Stockman, Fluorine-NMR experiments for high-throughput screening: theoretical aspects, practical considerations, and range of applicability, J. Am. Chem. Soc. 125 (25) (2003) 7696–7703, https://doi.org/10.1021/ja034646d.

[24] C. Dalvit, NMR methods in fragment screening: theory and a comparison with other biophysical techniques, Drug Discov. Today 14 (21) (2009) 1051–1057, https://doi.org/10.1016/j.drudis.2009.07.013.

[25] C. Dalvit, A. Vulpetti, Ligand-based fluorine NMR screening: principles and applications in drug discovery projects, J. Med. Chem. 62 (5) (2019) 2218–2244, https://doi.org/10.1021/acs.jmedchem.8b01210.

[26] F. Schipani, M. Manerba, R. Marotta, L. Poppi, A. Gennari, F. Rinaldi, A. Armirotti, F. Farabegoli, M. Roberti, G. Di Stefano, et al., The mechanistic understanding of RAD51 defibrillation: a critical step in BRCA2-mediated DNA repair by homologous recombination, Int. J. Mol. Sci. 23 (15) (2022), https://doi.org/10.3390/ijms23158338.

[27] E. Rajendra, A.R. Venkitaraman, Two modules in the BRC repeats of BRCA2 mediate structural and functional interactions with the RAD51 recombinase, Nucleic Acids Res. 38 (1) (2009) 82–96, https://doi.org/10.1093/nar/gkp873.

[28] Rinaldi, F.; Schipani, F.; Balboni, B.; Catalano, F.; Marotta, R.; Myers, S. H.; Previtali, V.; Veronesi, M.; Scietti, L.; Cecatiello, V.; et al. Isolation and Characterization of Monomeric Human RAD51: A Novel Tool for Investigating Homologous Recombination in Cancer. Angew. Chem. Int. Ed. n/a (n/a), e202312517. DOI: https://doi.org/10.1002/anie.202312517..

[29] T. Moschetti, T. Sharpe, G. Fischer, M.E. Marsh, H.K. Ng, M. Morgan, D.E. Scott, T. L. Blundell, V. A R, J. Skidmore, et al., Engineering archeal surrogate systems for the development of protein-protein interaction inhibitors against human RAD51, J. Mol. Biol. 428 (23) (2016) 4589–4607, https://doi.org/10.1016/j.jmb.2016.10.009.

[30] C. Dalvit, A. Parent, F. Vallée, M. Mathieu, A. Rak, Fast NMR methods for measuring in the direct and/or competition mode the dissociation constants of chemical fragments interacting with a receptor, ChemMedChem 14 (11) (2019) 1115–1127, https://doi.org/10.1002/cmdc.201900152.

[31] N. Arnoult, A. Correia, J. Ma, A. Merlo, S. Garcia-Gomez, M. Maric, M. Tognetti, C. W. Benner, S.J. Boulton, A. Saghatelian, et al., Regulation of DNA repair pathway choice in S and G2 phases by the NHEJ inhibitor CYREN, Nature 549 (7673) (2017) 548–552, https://doi.org/10.1038/nature24023.

[32] R. Buisson, J. Niraj, A. Rodrigue, C.K. Ho, J. Kreuzer, T.K. Foo, E.J.L. Hardy, G. Dellaire, W. Haas, B. Xia, et al., Coupling of homologous recombination and the checkpoint by ATR, Mol. Cell 65 (2) (2017) 336–346, https://doi.org/10.1016/j.molcel.2016.12.007.

[33] M.H. Tan, N.J. Nowak, R. Loor, H. Ochi, A.A. Sandberg, C. Lopez, J.W. Pickren, R. Berjian, H.O. Douglass Jr., T.M. Chu, Characterization of a new primary human pancreatic tumor line, Cancer Invest. 4 (1) (1986) 15–23, https://doi.org/10.3109/07357908609039823.
[34] G.S. Cowley, B.A. Weir, F. Vazquez, P. Tamayo, J.A. Scott, S. Rusin, A. East-Seletsky, L.D. Ali, W.F. Gerath, S.E. Pantel, et al., Parallel genome-scale loss of function screens in 216 cancer cell lines for the identification of context-specific genetic dependencies, Sci. Data 1 (2014) 140035, https://doi.org/10.1038/sdata.2014.35.
[35] C.J. Lord, A. Ashworth, PARP inhibitors: synthetic lethality in the clinic, Science 355 (6330) (2017) 1152–1158, https://doi.org/10.1126/science.aam7344.
[36] K.J. Dedes, P.M. Wilkerson, D. Wetterskog, B. Weigelt, A. Ashworth, J.S. Reis-Filho, Synthetic lethality of PARP inhibition in cancers lacking BRCA1 and BRCA2 mutations, Cell Cycle 10 (8) (2011) 1192–1199, https://doi.org/10.4161/cc.10.8.15273.
[37] W.H. Chen, J.S. Horoszewicz, S.S. Leong, T. Shimano, R. Penetrante, W.H. Sanders, R. Berjian, H.O. Douglass, E.W. Martin, T.M. Chu, Human pancreatic adenocarcinoma: in vitro and in vivo morphology of a new tumor line established from ascites, In Vitro 18 (1) (1982) 24–34, https://doi.org/10.1007/BF02796382.
[38] E.L. Deer, J. Gonzalez-Hernandez, J.D. Coursen, J.E. Shea, J. Ngatia, C.L. Scaife, M. A. Firpo, S.J. Mulvihill, Phenotype and genotype of pancreatic cancer cell lines, Pancreas 39 (4) (2010) 425–435, https://doi.org/10.1097/MPA.0b013e3181c15963.
[39] W.R. Gower Jr., R.M. Risch, C.V. Godellas, P.J. Fabri, HPAC, a new human glucocorticoid-sensitive pancreatic ductal adenocarcinoma cell line, In Vitro Cell Dev. Biol. 30A (3) (1994) 151–161, https://doi.org/10.1007/BF02631438.
[40] E.H. Baugh, H. Ke, A.J. Levine, R.A. Bonneau, C.S. Chan, Why are there hotspot mutations in the TP53 gene in human cancers? Cell Death Differ. 25 (1) (2018) 154–160, https://doi.org/10.1038/cdd.2017.180.
[41] W. Wu, X. Liu, L. Wei, T. Li, Y. Zang, Y. Qian, T. Bai, J. Li, M. Xie, Y. Zhu, et al., Tp53 mutation inhibits ubiquitination and degradation of WISP1 via down-regulation of Siah1 in pancreatic carcinogenesis, Front. Pharmacol. 9 (2018) 857, https://doi.org/10.3389/fphar.2018.00857.
[42] S.M. Hoy, Talazoparib: first global approval, Drugs 78 (18) (2018) 1939–1946, https://doi.org/10.1007/s40265-018-1026-z.
[43] A. Kachmazov, L. Bolotina, A. Kornietskaya, O. Kuznetsova, M. Ivanov, A. Fedenko, Complete response to talazoparib in patient with pancreatic adenocarcinoma harboring somatic PALB2 mutation: a case report and literature review, Front. Oncol. 12 (2022) 953908, https://doi.org/10.3389/fonc.2022.953908.
[44] J.J. Gruber, A. Afghahi, K. Timms, A. DeWees, W. Gross, V.N. Aushev, H.-T. Wu, M. Balcioglu, H. Sethi, D. Scott, et al., A phase II study of talazoparib monotherapy in patients with wild-type BRCA1 and BRCA2 with a mutation in other homologous recombination genes, Nat. Can. (Ott.) 3 (10) (2022) 1181–1191, https://doi.org/10.1038/s43018-022-00439-1.
[45] T.A. Leal, M.N. Sharifi, N. Chan, R. Wesolowski, A.A. Turk, J.Y. Bruce, R. M. O'Regan, J. Eickhoff, L.M. Barroilhet, J. Malhotra, et al., A phase I study of talazoparib (BMN 673) combined with carboplatin and paclitaxel in patients with advanced solid tumors (NCI9782), Cancer Med. 11 (21) (2022) 3969–3981, https://doi.org/10.1002/cam4.4724.
[46] B. Wang, D. Chu, Y. Feng, Y. Shen, M. Aoyagi-Scharber, L.E. Post, Discovery and characterization of (8S,9R)-5-Fluoro-8-(4-fluorophenyl)-9-(1-methyl-1H-1,2,4-triazol-5-yl)-2,7,8,9-tetrahydro-3H-pyrido[4,3,2-de]phthalazin-3-one (BMN 673, talazoparib), a novel, highly potent, and orally efficacious poly(ADP-ribose) polymerase-1/2 inhibitor, as an anticancer agent, J. Med. Chem. 59 (1) (2016) 335–357, https://doi.org/10.1021/acs.jmedchem.5b01498.
[47] Y. Shen, M. Aoyagi-Scharber, B. Wang, Trapping poly(ADP-ribose) polymerase, J. Pharmacol. Exp. Therapeut. 353 (3) (2015) 446–457, https://doi.org/10.1124/jpet.114.222448.
[48] S. Boussios, C. Abson, M. Moschetta, E. Rassy, A. Karathanasi, T. Bhat, F. Ghumman, M. Sheriff, N. Pavlidis, Poly (ADP-Ribose) polymerase inhibitors: talazoparib in ovarian cancer and beyond, Drugs R 20 (2) (2020) 55–73, https://doi.org/10.1007/s40268-020-00301-8.
[49] J. Murai, S.Y. Huang, B.B. Das, A. Renaud, Y. Zhang, J.H. Doroshow, J. Ji, S. Takeda, Y. Pommier, Trapping of PARP1 and PARP2 by clinical PARP inhibitors, Cancer Res. 72 (21) (2012) 5588–5599, https://doi.org/10.1158/0008-5472.can-12-2753.
[50] A.C. Carley, M. Jalan, S. Subramanyam, R. Roy, G.E.O. Borgstahl, S.N. Powell, Replication protein A phosphorylation facilitates RAD52-dependent homologous recombination in BRCA-deficient cells, Mol. Cell Biol. 42 (2) (2022) 1–17, https://doi.org/10.1128/mcb.00524-21.
[51] K. Hanamshet, A.V. Mazin, The function of RAD52 N-terminal domain is essential for viability of BRCA-deficient cells, Nucleic Acids Res. 48 (22) (2020) 12778–12791, https://doi.org/10.1093/nar/gkaa1145.
[52] B.A. Carneiro, W.S. El-Deiry, Targeting apoptosis in cancer therapy, Nat. Rev. Clin. Oncol. 17 (7) (2020) 395–417, https://doi.org/10.1038/s41571-020-0341-y.
[53] C.J.F. Van Noorden, The history of Z-VAD-FMK, a tool for understanding the significance of caspase inhibition, Acta Histochem. 103 (3) (2001) 241–251, https://doi.org/10.1078/0065-1281-00601.
[54] L. Cao, W. Mu, Necrostatin-1 and necroptosis inhibition: pathophysiology and therapeutic implications, Pharmacol. Res. 163 (2021) 105297, https://doi.org/10.1016/j.phrs.2020.105297.
[55] M.A.G. Barbosa, C.P.R. Xavier, R.F. Pereira, V. Petrikaitė, M.H. Vasconcelos, 3D cell culture models as recapitulators of the tumor microenvironment for the screening of anti-cancer drugs, Cancers 14 (1) (2022) 190.
[56] F. Pampaloni, E.G. Reynaud, E.H. Stelzer, The third dimension bridges the gap between cell culture and live tissue, Nat. Rev. Mol. Cell Biol. 8 (10) (2007) 839–845, https://doi.org/10.1038/nrm2236.
[57] S. Roche, F. O'Neill, J. Murphy, N. Swan, J. Meiller, N.T. Conlon, J. Geoghegan, K. Conlon, R. McDermott, R. Rahman, et al., Establishment and characterisation by expression microarray of patient-derived xenograft panel of human pancreatic adenocarcinoma patients, Int. J. Mol. Sci. 21 (3) (2020), https://doi.org/10.3390/ijms21030962.
[58] S.R. Nelson, C. Zhang, S. Roche, F. O'Neill, N. Swan, Y. Luo, A. Larkin, J. Crown, N. Walsh, Modelling of pancreatic cancer biology: transcriptomic signature for 3D PDX-derived organoids and primary cell line organoid development, Sci. Rep. 10 (1) (2020) 2778, https://doi.org/10.1038/s41598-020-59368-7.